

## Advanced Magnetic Resonance Imaging of the Physical Processes in Human Glioblastoma

Jayashree Kalpathy-Cramer<sup>1,2</sup>, Elizabeth R. Gerstner<sup>3</sup>, Kyrre E. Emblem<sup>1,4</sup>, Ovidiu C. Andronesi<sup>1,2</sup>, and Bruce Rosen<sup>1,2</sup>

### Abstract

The most common malignant primary brain tumor, glioblastoma multiforme (GBM) is a devastating disease with a grim prognosis. Patient survival is typically less than two years and fewer than 10% of patients survive more than five years. Magnetic resonance imaging (MRI) can have great utility in the diagnosis, grading, and management of patients with GBM as many of the physical manifestations of the pathologic processes in GBM can be visualized and quantified using MRI. Newer MRI techniques such as dynamic contrast enhanced and dynamic susceptibility contrast MRI provide functional information about the tumor hemodynamic status. Diffusion MRI can shed light on tumor cellularity and the disruption of white matter tracts in the proximity of tumors. MR spectroscopy can be used to study new tumor tissue markers such as IDH mutations. MRI is helping to noninvasively explore the link between the molecular basis of gliomas and the imaging characteristics of their physical processes. We, here, review several approaches to MR-based imaging and discuss the potential for these techniques to quantify the physical processes in glioblastoma, including tumor cellularity and vascularity, metabolite expression, and patterns of tumor growth and recurrence. We conclude with challenges and opportunities for further research in applying physical principles to better understand the biologic process in this deadly disease.

**See all articles in this *Cancer Research* section, "Physics in Cancer Research."**

*Cancer Res*; 74(17); 4622–37. ©2014 AACR.

### Introduction

Primary brain tumors encompass a spectrum of diseases that, in the landscape of cancer, are less common but unfortunately often carry a grim prognosis. The most common malignant primary brain tumor is glioblastoma multiforme (GBM) and despite aggressive treatment with surgery, radiation, and chemotherapy, patient survival is typically <2 years and <10% of patients survive >5 years (1–5). Magnetic resonance imaging (MRI) plays an important role in understanding GBM tumor biology and response to treatment because MRI is already a part of routine clinical practice, and recent advances in imaging can now capture a variety of anatomic and physiologic processes (5–10).

GBMs are well visualized on MRI because they profoundly disrupt normal tissue architecture. These tumors are densely

cellular and widely infiltrate into normal brain. The pathologic hallmark of GBM is the increased expression of proangiogenic cytokines (e.g., vascular endothelial growth factor, VEGF) leading to the formation of highly abnormal tumor vasculature characterized by hyperpermeable vessels (Fig. 1A), increased vessel diameter, and heterogeneous tumor blood flow (5, 11). Some areas of tumor receive too much blood flow and other areas do not receive enough blood flow, resulting in areas of hypoxia (12, 13). The hyperpermeable blood vessels allow fluid to leak from the intravascular space to the extravascular space, producing significant peritumoral edema (11, 13, 14). All of these pathologic processes—tumor cell density, abnormal tumor vasculature, and peritumoral edema—can be studied, and more importantly quantitated, using MRI (13, 15–24).

This abnormal tumor vasculature is an important therapeutic target and, thus, being able to noninvasively measure vascular response to therapy is critical to advancing treatment for this challenging disease (25). The exact mechanisms thought to underlie the benefits of antiangiogenic agents, such as bevacizumab, the only FDA-approved drug for recurrent GBM, remain unclear. Current thinking centers around the "vascular normalization hypothesis" (26, 27), in which antiangiogenic agents act to prune tumor vessels into a more "normal" vasculature rather than causing tumor starvation through decreased blood flow as seen in Fig. 1B. A more "normal" tumor vasculature includes reduction of abnormal vessel diameters, increased pericyte coverage, and more normal basement membranes. Normalization is thought to result in reduced vessel permeability and improved blood flow (28).

<sup>1</sup>Athinoula A. Martinos Center for Biomedical Imaging, Massachusetts General Hospital and Harvard Medical School, Charlestown, Massachusetts. <sup>2</sup>Department of Radiology, Massachusetts General Hospital and Harvard Medical School, Boston, Massachusetts. <sup>3</sup>Department of Neurology, Massachusetts General Hospital and Harvard Medical School, Boston, Massachusetts. <sup>4</sup>The Intervention Centre, Oslo University Hospital, Oslo, Norway.

J. Kalpathy-Cramer and E.R. Gerstner contributed equally to this article.

**Corresponding Author:** Jayashree Kalpathy-Cramer, Massachusetts General Hospital/Harvard Medical School, 149 13th Street, Charlestown, MA 02129. Phone: 617-724-4657; Fax: 617-726-7422; E-mail: kalpathy@nmr.mgh.harvard.edu

doi: 10.1158/0008-5472.CAN-14-0383

©2014 American Association for Cancer Research.

This allows more effective delivery of cytotoxic therapies (e.g., chemotherapy) to parts of the tumor previously underperfused and drastically decreases peritumoral edema (29). Newer MRI techniques providing functional information on tumor hemodynamic status, in particular dynamic contrast enhanced (DCE) or dynamic susceptibility contrast (DSC) MRI, can shed light on the impact antiangiogenic drugs have on tumor vasculature and so are key tools to study tumor biology and aid in drug development (24, 25, 30–32).

Finally, recent insights into the molecular heterogeneity of GBMs and other gliomas have led to a larger shift in thinking about the classification of gliomas. New tumor tissue markers such as isocitrate dehydrogenase (IDH) mutations (33) and novel drugs that target receptor tyrosine kinases are being explored (for instance, cediranib, cabozantinib, erlotinib, sunitib, and others; refs. 34–36). MRI is rapidly catching up with these tissue-based advances and helping to noninvasively explore the link between the molecular basis of gliomas and the imaging characteristics of their physical processes.

In this review, we cover several MRI-based imaging techniques and highlight the application of these techniques to quantify many of the physical processes in glioblastoma such as tumor cell density, vascular structure, oxygenation status, metabolite and growth factor expression, and patterns of tumor proliferation and infiltration. Finally, we discuss the current limitations and challenges of these techniques and identify potential areas for the application of physical principles to better understanding the biologic processes in this deadly disease.

### Application of MR Physics to Glioblastoma

In most clinical applications, the MRI signal originates from the hydrogen nucleus, which is a single proton. A strong static magnetic field ( $B_0$ ) aligns the nuclear spins and creates macroscopically longitudinal magnetization due to difference between spin-up and spin-down populations. A radiofrequency field ( $B_1$ ) induces transitions between the spin-up and spin-down orientations, which result in macroscopically transverse magnetization precessing around the static field at a frequency known as the Larmor frequency. For a given nucleus, the Larmor frequency is proportional to the external field by the gyromagnetic ratio.

The MRI signal is influenced by several tissue-specific factors, which enables a multitude of image contrasts, making MRI a tool that can probe physiologic processes as minute as intracellular water diffusion and vessel size. A brief overview of the main players—relaxation, magnetic susceptibility, electron screening, chemical shift, and diffusion—is given below.

#### Relaxation and signal contrast

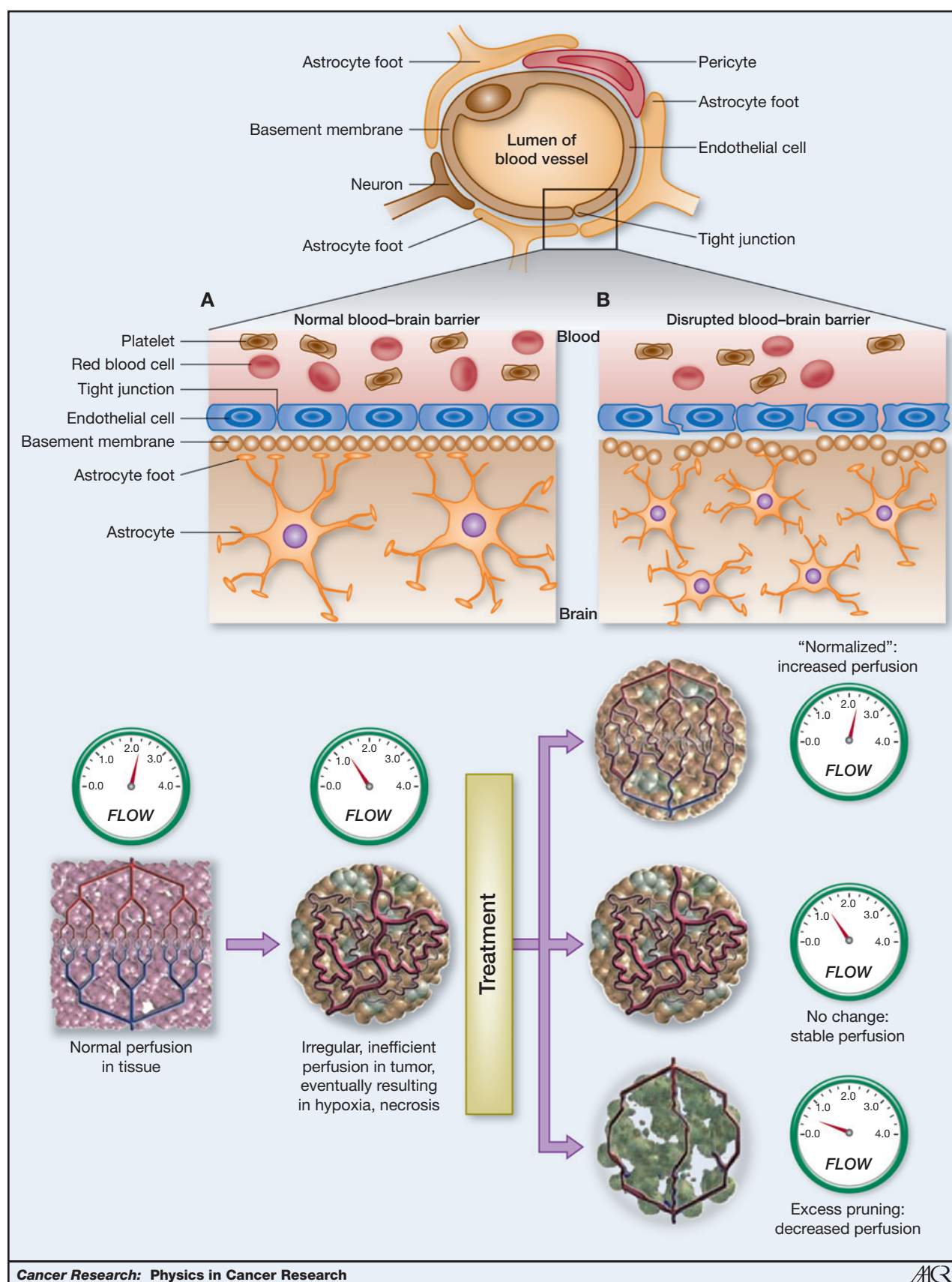
MRI is known for its excellent soft tissue signal contrast (37). A crucial mechanism that allows for signal contrast among different tissues types is nuclear magnetic relaxation. Relaxation describes the process in which the protons return to their equilibrium state after excitation by a radiofrequency (RF) pulse. Two separate relaxation processes are identified, each with their specific time constant: T1 longitudinal relaxation, describing the return to the equilibrium state toward

the recovery of longitudinal magnetization, and T2 transverse relaxation, a measure for the decay of transverse magnetization and MRI signal in the transverse plane. Relaxation is tissue-type specific, and by controlling the timing of the RF pulses, one can manipulate the resulting signal. For example, rapid successive RF pulses do not allow full relaxation back to equilibrium for tissues with long T1 (e.g., gray matter), whereas tissues with shorter T1 (e.g., white matter) will be back in equilibrium before every new RF pulse. Such an MRI sequence will, therefore, generate larger signals from regions with shorter T1, and yield a so-called T1-weighted image, which enables the visualization of white/gray matter contrast.

T1 and T2 relaxation are, therefore, the naturally present signal contrast mechanism and can be used to visual normal anatomy and pathologic changes (37, 38). However, as the intrinsic changes in T1 and T2 relaxation due to disease processes can be quite subtle, to achieve more pronounced contrast in MR images, exogenous contrast agents (CA) can be used. In clinical oncology MRI studies, low-molecular weight gadolinium-based CA such as gadopentetate dimeglumine, gadolinium diethylenetriaminepentaacetic acid or Gd-DTPA are commonly used. These agents locally shorten the T1 relaxation times, and allow for better contrast between regions with and without the CA and are commonly used because of the greatly enhanced ability to detect and delineate tumors. The blood–brain barrier (BBB) in the healthy brain restricts the CA to the vascular bed. However, disruption of the BBB in the presence of intraaxial tumors (11, 13, 39) can lead to the accumulation of these agents in the interstitial spaces surrounding the leaky vasculature, resulting in increased signal intensity on T1-weighted MR images (37). This phenomenon can be used to qualitatively observe the level of signal enhancement in the tumor as a surrogate measure of malignancy.

Advanced MR techniques such as DCE-MRI allow us to quantify these changes in tumor vasculature in addition to qualitatively assessing the level of enhancement (40–42). The underlying principles of DCE-MRI are based on the exchange of these gadolinium-based, exogenous CAs between the intravascular compartment and the interstitial tissue as shown by the schematic in Fig. 2A. DCE-MRI is accomplished by measuring the time course of this CA as it diffuses from the blood pool into tissues through leaky blood vessels. Typically, a set of dynamic T1-weighted baseline images are acquired before the CA injection, and the imaging is continued as the CA is taken up in the tissue and finally through a washout phase as seen in Fig. 2B. The postcontrast T1-weighted image can be seen in Fig. 2C. The shape of this signal time course in the voxels or larger regions of interest (ROI) provides information about the flow and permeability of the vasculature and the microenvironment of the tumor.

A variety of approaches, parametric, semiparametric, and nonparametric (43–49), have been used to characterize these curves. Nonparametric approaches (50, 51) include measuring the slope of the rising portion of the curve, measuring the area under the curve at a fixed time point, and measuring the maximum and equilibrium portions of the curve. In the





parametric approaches, the CA transport phenomena in the highly complex microenvironment have been simplified using pharmacokinetic (PK) approaches for DCE-MRI assessment. These PK models, proposed in the 1990s, first convert the signal to a concentration of the CA and then fit a nonlinear function to this concentration in tissue (32, 40, 45, 52). By assuming or measuring the time course of the CA signal in the vessels (the arterial input function, AIF), these models, typically known as "Tofts models," estimate two primary parameters:  $K_{trans}$ , the volume transfer coefficient, and  $v_e$ , the extracellular, extravascular space (the fractional volume of distribution for the CA outside the vessels). In the original Tofts model (40), it was shown that under flow-limited conditions,  $K_{trans}$  reflected blood flow, whereas under permeability-limited conditions,  $K_{trans}$  was a measure of the permeability surface area product per unit volume of tissue. Extensions to the Tofts model to account for the portion of the signal arising from the intravascular component have been developed by adding a term containing the vascular volume fraction ( $v_p$ ) to the model (40, 53, 54). An example map of the  $K_{trans}$  can be seen in Fig. 2D. DCE-MRI is most useful, therefore, in studying at vascular leakiness and tumor microenvironment and has great potential to be used in monitoring the changes in the leakiness of the vasculature arising from antiangiogenic therapies (25, 27, 45).

### Magnetic susceptibility

The magnetic susceptibility is a measure of how a material responds to an applied magnetic field. Most tissues are slightly diamagnetic, meaning that within the tissue, a field in the opposite direction of the externally applied magnetic field is generated (55). The net magnetic field in tissue is, therefore, somewhat smaller than the applied magnetic field. In paramagnetic materials, the opposite effect occurs and the magnetic field is enhanced inside the paramagnetic material. An important notion with respect to susceptibility is that it acts nonlocally: the susceptibility at a certain location influences the magnetic field not only in but also around that location. At interfaces of regions with different susceptibilities, e.g., interfaces between tissue and air or areas where a paramagnetic CA is present in the diamagnetic tissue, field inhomogeneities are present. The strength of these inhomogeneities depends on the susceptibility difference as well as the spatial distribution of the susceptibilities. For example, when image pixels are comparable with the spatial extent of susceptibility anisotropy, this manifests as signal loss in those areas due to the incoherent dephasing of transverse magnetization in an inhomogeneous field ( $T_2^*$  relaxation). Therefore, knowledge about these field disturbances contains information about the tissue microenvironment, through, for instance, the spatial

distribution of CA. This is an important effect that is used in vessel size measurements with Dynamic Susceptibility Contrast (DSC) MRI sequences.

In perfusion DSC-MRI (56–58), a CA is injected and a time series of images of the first-pass passage of the CA through the brain is acquired. In DSC,  $T_2$ - or  $T_2^*$ -weighted images are acquired and the signal loss due to the susceptibility effect of the paramagnetic contrast, as seen on the signal intensity–time curve, is measured as seen in Fig. 3A. The corresponding postcontrast  $T_1$ -weighted image and FLAIR image showing areas of contrast enhancement and edema, respectively, can be seen in Fig. 3B and C. This reduction in the signal recorded during the first pass of the CA depends on the architecture of the vessels and the particular sequences used for the acquisition. The signal time curve data are processed, using tracer dilution theory (59), to generate maps of perfusion-related parameters such as relative cerebral blood volume (rCBV), relative cerebral blood flow (rCBF), and the mean transit time (MTT). An example of an rCBF and rCBV maps can be as shown in Fig. 3D and E. These properties form the central volume principle, stating that the blood volume of tissue is equal to the blood flow multiplied by the MTT through the capillary tissue (60).

In brief, a relaxation rate curve ( $\Delta R_2^*$ ) proportional to the contrast concentration-versus-time curve is used and converted from the signal intensity-versus-time under the assumption of a linear relationship between the observed signal change and the CA concentration in capillary tissue (60). From this, rCBV is proportional to the integral of the  $\Delta R_2^*$  curve, whereas measures of CBF and MTT can be derived by scaling the tissue-specific  $\Delta R_2^*$  curve with that of a feeding artery, the AIF (60, 61). An advantage of DSC-MRI is high CA sensitivity combined with high temporal resolution (62). A second advantage is the long-reaching  $T_2^*$  effect that influences a large portion of extravascular water protons in the brain (63) and sufficient image contrast is, therefore, not limited to areas of BBB breakdown, unlike in DCE-MRI.

A further benefit of DSC-MRI is the ability to indirectly measure microvessel calibers by use of a technique commonly referred to as vessel size MRI. During the 1990s, Rosen and colleagues (56–58) at Massachusetts General Hospital demonstrated that diameters of tubes or vessels containing susceptibility-inducing agents could be differentiated by their magnetic susceptibility and that using a combination of gradient-echo ( $T_2^*$  sensitive) and spin-echo ( $T_2$  sensitive) MR imaging techniques could provide a voxel-by-voxel estimate of relative vessel diameters in tissue (58, 64–68). By use of a simultaneous gradient-echo spin-echo image acquisition, vessel caliber MRI is performed by measuring the changes in  $R_2^*$  and  $R_2$ , respectively, from the first pass of the CA (Fig. 3F). Here, the spin-echo MRI sequence is selectively sensitive to small

**Figure 1.** Tumor vasculature. A, the healthy BBB protects the brain through a network of astrocytes, pericytes, endothelial cells, and neurons that form tight, impermeable junctions, which exclude large cells, macromolecules, and excess fluid from the central nervous system. The disruptions in the BBB that occur in brain tumors result in a thickened and disrupted basement membrane and widened junctions that allow passage of macromolecules and fluid (adapted from Gerstner et al. VEGF inhibitors in the treatment of cerebral edema in patients with brain cancer. *Nat Rev Clin Oncol* 2009;6:229–36). B, vascular normalization hypothesis. Schematic of the effects of antiangiogenic therapy (adapted from Sorensen et al.; ref. 27).

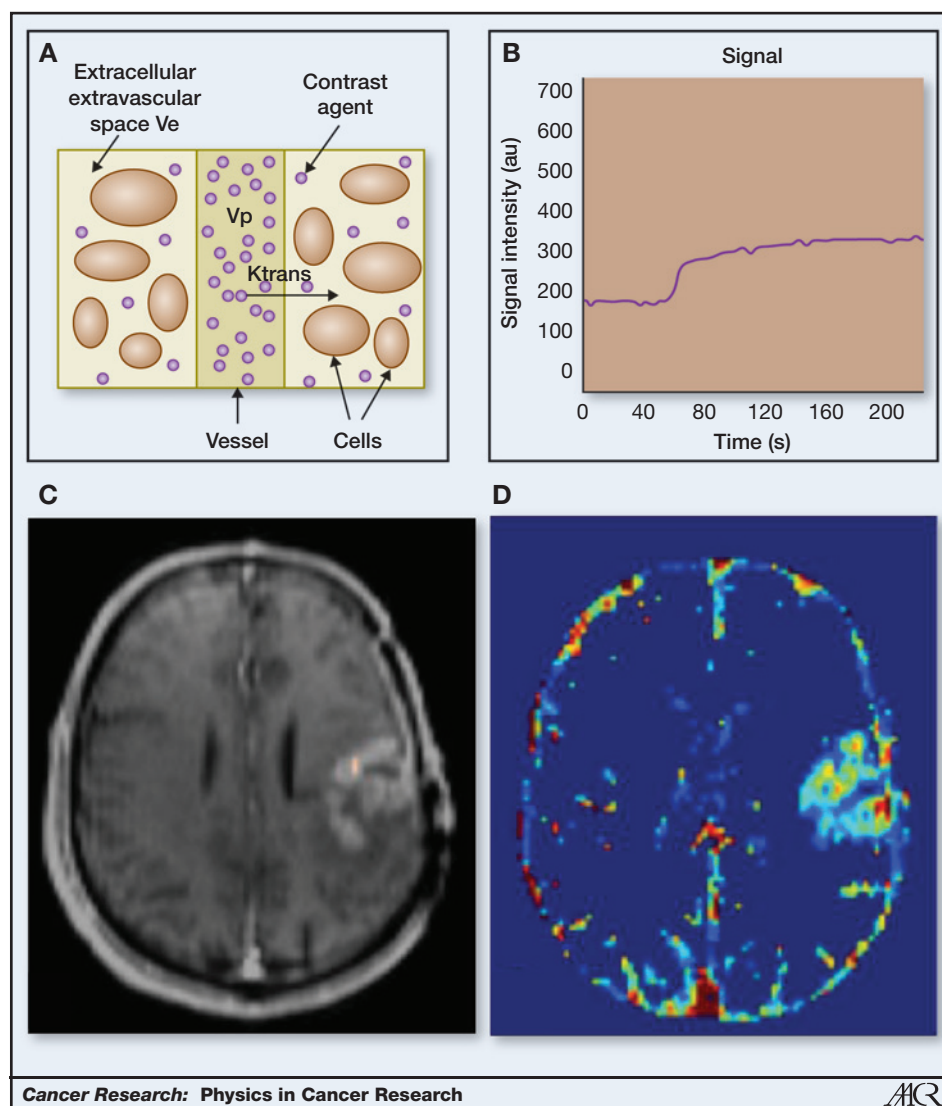


Figure 2. DCE imaging. A, schematic of DCE compartments including the vascular bed, cells, and EES. Adapted from Parker and Padhani (37).  $T_1$ -W DCE-MRI:  $T_1$ -Weighted Dynamic Contrast-Enhanced MRI. In: Tofts P, editor. Quantitative MRI of the Brain. Copyright 2003 John Wiley & Sons, Ltd. B, DCE signal in the contrast-enhancing tumor region of interest. C, example of postcontrast  $T_1$  image highlights tumor due to CA extravasation. D,  $K_{trans}$  map created by fitting the "Tofts" model to the DCE-MRI signal.

vessels ( $<10\ \mu\text{m}$ ), whereas the gradient-echo MRI sequence is sensitive to both small and larger vessels (66).

### Diffusion of water

Diffusion describes the microscopic random displacement of molecules (69–72). Diffusive movement of water through an inhomogeneous magnetic field affects the proton resonance frequencies and, thus, the phase of the signal, leads to so-called dephasing, and ultimately causes signal loss. The larger the displacement of the protons through an inhomogeneous field, the more signal loss occurs. This principle is the basis of diffusion MRI techniques, in which the MRI signal is deliberately made sensitive to diffusive water motion by controlled application of magnetic field inhomogeneities. These applied inhomogeneities are captured in the  $b$  value, where higher  $b$  values represent stronger inhomogeneities. The larger the displacement of the protons in water molecules through an inhomogeneous field, the more signal loss occurs; so, significant signal loss is expected from

areas where water is able to diffuse over large distances (e.g., in the ventricles) and less so in areas where the diffusion is restricted (e.g., in highly cellular tissue).

In the context of clinical MRI in oncology, this process is greatly influenced by the geometry and structure of the micro-environment of the tissue and provides the ability of MR to probe dimensions that are much smaller than the voxel size, i.e., the unit of volume measured in the MR image, which is typically in millimeters. Most commonly used in clinical practice is the notion of an "apparent diffusion coefficient" or ADC. The signal attenuation or loss seen in biologic tissues is dependent on the strength of the magnetic field gradient, the duration of the gradient, and the time between the application of two gradients (the "diffusion time"), all of which are, again, reflected in the " $b$  value." Clinical scans typically use two or more " $b$  values" (often 0 and  $1,000\ \text{s/mm}^2$  reflecting the time (seconds) water diffuses within a particular area ( $\text{mm}^2$ ). The ADC is calculated from the signal attenuation seen at increasing  $b$  values assuming a monoexponential signal attenuation

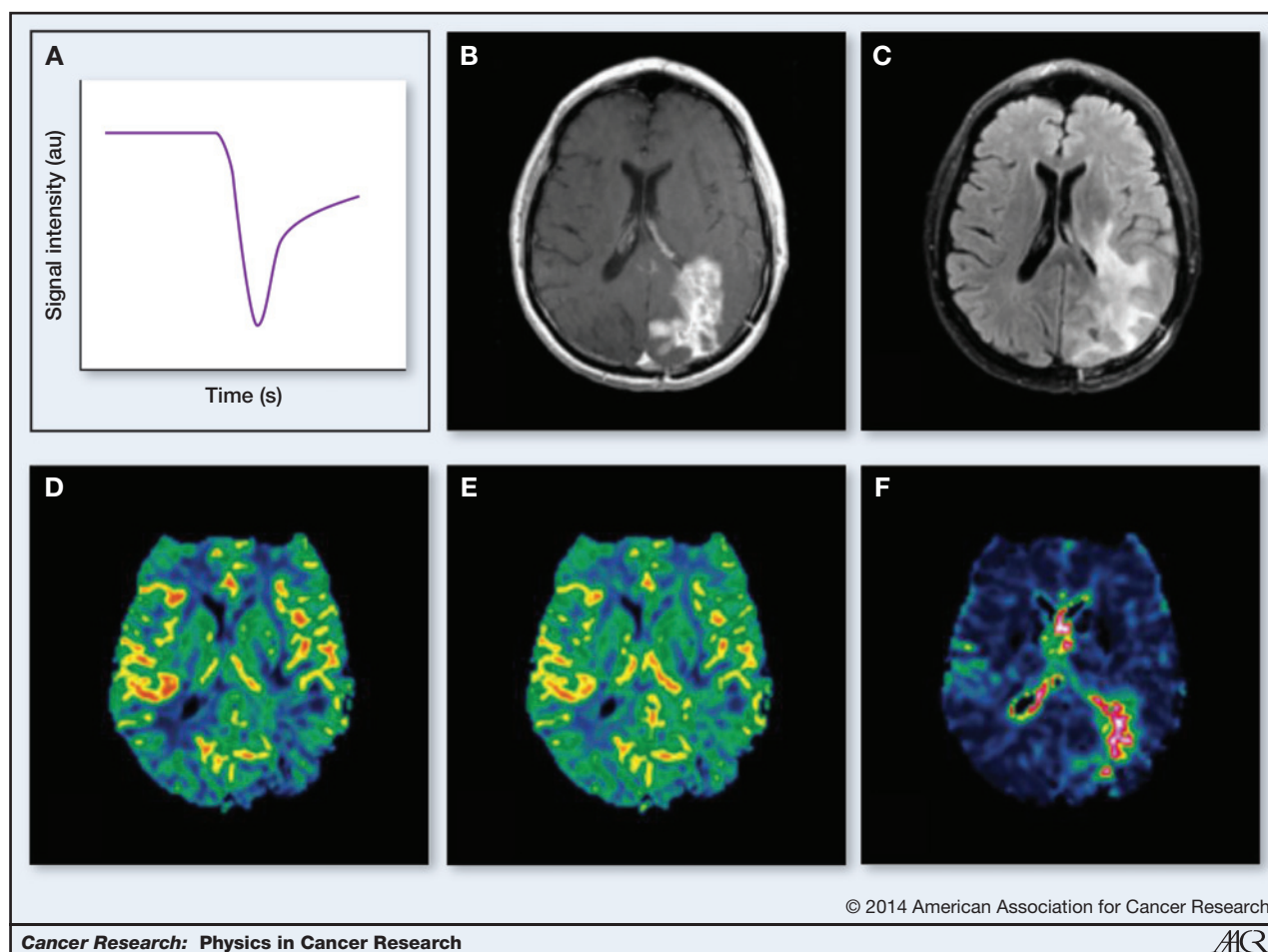


**Figure 3.** DSC imaging. A, example DSC signal ( $T_2^*$ ) in GBM shows the drop in signal intensity as the bolus of CA passes through. B, T1 postcontrast image shows areas of contrast-enhancing tumor. C, FLAIR image shows areas of edema. D, color map of rCBF created using DSC analysis. E, color map of rCBV created using DSC analysis. F, color map of vessel size imaging created using DSC analysis.

curve of signal intensity, again the " $b$  value" as seen in Fig. 4A. Figure 4B and C shows sample slices of FLAIR and postcontrast-enhanced T1-weighted image showing areas of edema and contrast enhancement. Figure 4D–F displays the equivalent diffusion-weighted (DW) image, ADC map, and color fractional anisotropy (FA) map.

MRI diffusion measurements can provide information about the tissue architecture, tumor microenvironment and size, orientation, and structure of the intra- and extracellular spaces and have been used to quantify edema, estimate tumor cell density, and quantify restricted diffusion due to cell proliferation or hypoxia (8, 19, 73–75). As DW-MRI does not require the use of intravenous contrast media, it can be used in patients with compromised renal functions, a distinct advantage over contrast-enhanced MRI.

#### Electron screening and chemical shift

The proton resonance frequency is linearly proportional to the magnetic field experienced by the proton. In the previous section, it became clear that the susceptibility of a material affects the magnetic field inside and around that material once

it is placed in an external magnetic field. There is an additional effect, which determines the net magnetic field at the proton level: the electron cloud around the nucleus. This electron cloud leads to an effective screening of the magnetic field. Depending on the molecular orbits, this screening can be weak or strong, which is described by the proton electron screening constant. The fact that the proton electron screening constant differs for different molecular configurations is used in MR spectroscopy (MRS), where specific molecular compounds can be detected and quantified by measuring their resonance frequencies in a certain region in the tissue. A term closely related to electron screening is chemical shift, which is defined as the difference in screening constant between the molecule of interest and a reference standard, and rendered field independent by taking the ratio of the difference to Larmor frequency.

MRS has been used for almost three decades to probe tissue for markers of metabolism (76, 77). MRS measures brain metabolites based on their unique spectra originating from nuclei such as proton ( $^1\text{H}$ ), phosphorus ( $^{31}\text{P}$ ), and carbon ( $^{13}\text{C}$ ). Steady-state levels of metabolites are most commonly measured with  $^1\text{H}$ -MRS (78), whereas with  $^{13}\text{C}$ -MRS (79) and



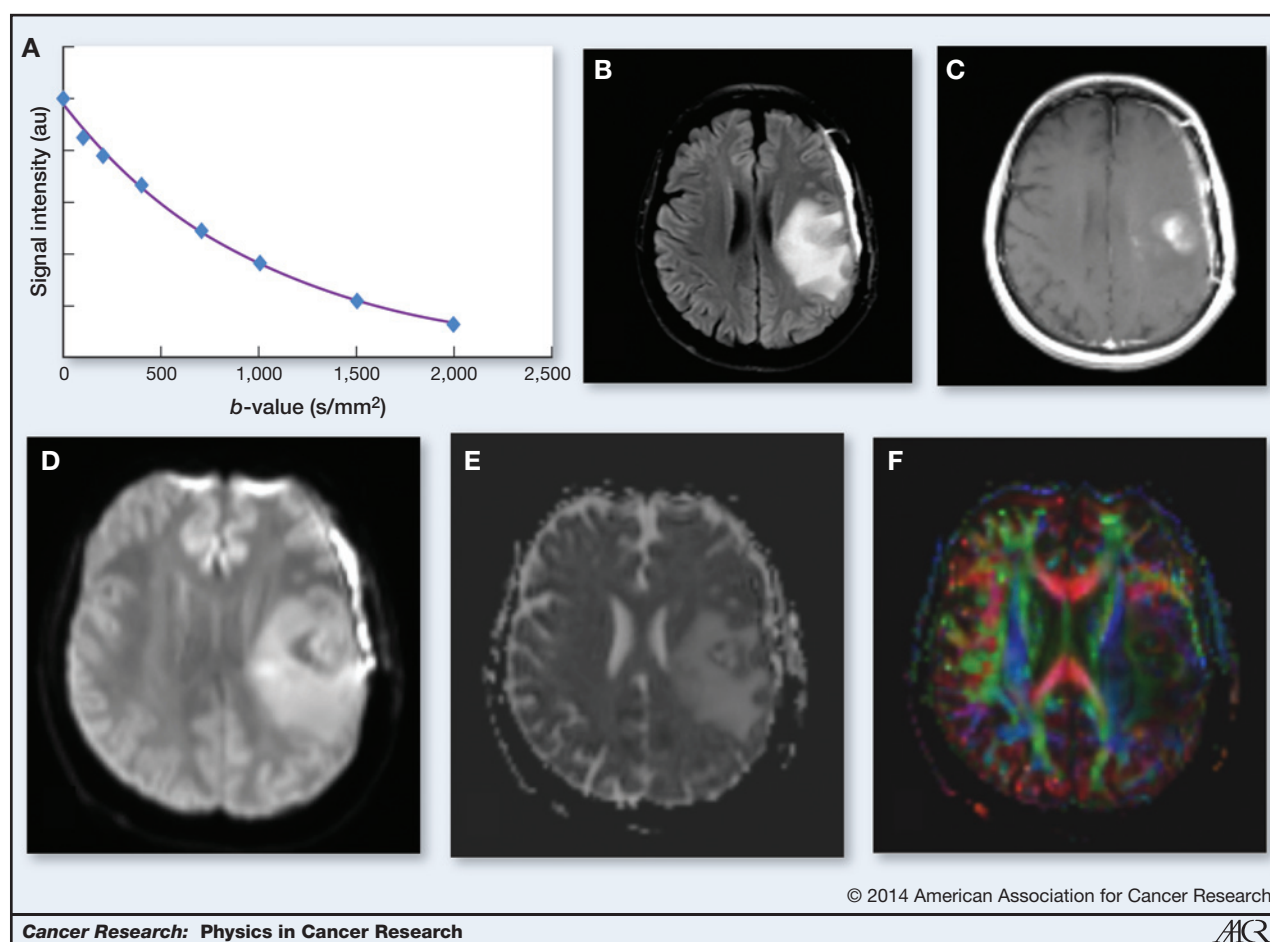


**Figure 4.** Diffusion imaging. A, DW images acquired at different  $b$  values show an exponential attenuation of the signal. The ADC can be estimated from this curve B, FLAIR image allows the visualization of edema C, enhancing tumor seen on postcontrast T1-weighted image D, DW image. E, ADC map shows increased ADC in areas of edema and areas of low ADC in areas of contrast-enhancing tumor. F, color FA map showing the loss of white matter tracts in areas of peritumoral edema.

$^{31}\text{P}$ -MRS (80) dynamic measurements can be performed to investigate kinetics of the tricarboxylic acid (TCA) cycle and ATP production. Metabolites detected with  $^1\text{H}$ -MRS in brain cancers include, among others, N-acetyl aspartate (NAA), choline, creatine, myo-inositol, glutamate and glutamine, lactate and recently, 2-hydroxyglutarate (2HG).  $^{31}\text{P}$ -MRS detects ATP, ADP, AMP, phosphocreatine, and phospholipids. Because of a low innate abundance of carbon,  $^{13}\text{C}$ -MRS requires infusion of labeled  $^{13}\text{C}$ -labeled compounds such as glucose (81), acetate (82), pyruvate (83), or fumarate (84), which can be used to investigate the dynamics of the TCA cycle. More recently, the use of hyperpolarization methods have been able to significantly increase the signal-to-noise ratio of  $^{13}\text{C}$ -MRS, and has shown promise for imaging enzymatic reactions *in vivo* (85, 86). With more development to extend the imaging time of hyperpolarized agents (87, 88), dynamic  $^{13}\text{C}$ -MRS may become a very powerful method for cancer researchers and clinical oncologists. In addition to *in vivo* MRS, *ex vivo* MRS on biopsies can provide a wealth of information, and in the case of high-resolution magic angle spinning (HRMAS; ref. 89), it is a completely nondestructive method to obtain the detailed

metabolic profile—a key benefit in a disease where tumor tissue is precious because of the challenges of brain surgery.

For oncologic applications, MRS has been used for initial differential diagnosis, to grade tumors (90), plan treatment and monitor response (91), or visualize drug delivery with  $^{19}\text{F}$ -labeled compounds (92). Although the histo/molecular/genopathologic examinations of tumor specimens constitute the gold-standard for definitive diagnosis and grading of tumors, MRS can provide useful biomarkers to monitor treatment. In this regard, MRS can help disambiguate the puzzles of pseudo/true-progression and pseudo/true-response (93) that are clinically very relevant and often may be difficult to distinguish.

### Advanced MRI in Monitoring Physical and Biologic Processes in Glioblastoma

#### Tumor detection, diagnosis, and grading

DSC-MRI, DCE-MRI, DW-MRI, and MRS have all demonstrated utility in the detection, diagnosis, and grading of tumors. DSC-MRI may be helpful in determining histologic grade of gliomas before surgery (31, 94–97) and has demonstrated

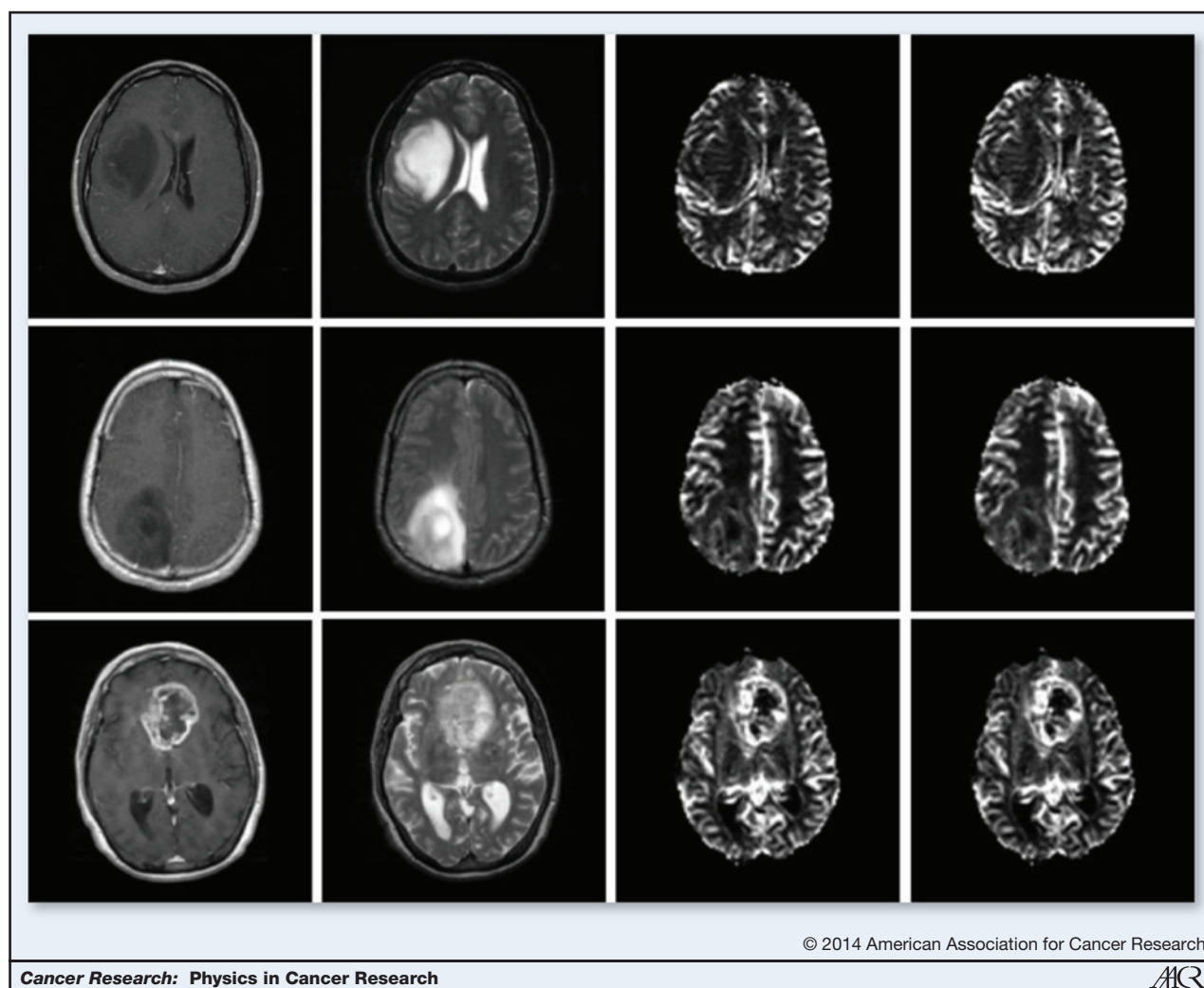


Figure 5. Grading tumors using DSC-MRI; left to right, postcontrast T1, T2, rCBF, and rCBV images of grade 2 (top), grade 3 (middle), and grade 4 (bottom) tumors generated using DSC-MRI. Note the absence of contrast enhancement in the grade 2 and grade 3 tumors. Also, note the elevated rCBV and rCBF in the grade 4 tumors.

improved sensitivity and predictive value compared with standard contrast-enhanced MRI (98–100). Low-grade tumors typically do not exhibit elevated rCBV, whereas high-grade gliomas do (101), as seen in Fig. 5. This information may be helpful in targeting a surgical biopsy to the area of most concern if a complete resection is not safe. Recent work has demonstrated that transforming low-grade gliomas show signs of increased rCBV up to 1 year earlier than contrast enhancement is apparent on T1-weighted MRI (102). This change in rCBV may reflect the angiogenic switch representing malignant transformation.

DCE-MRI (103–104) has similarly been used to grade tumors, as generally more vascular, leaky gliomas are more likely to be higher grade. However, DCE-MRI has not yet gained widespread clinical use because of challenges in acquisition and analysis techniques. Diffusion imaging has also been used to localize and grade tumors (105), separate glioblastomas from metastases (106), and in surgical mapping before tumor resection (107–108).

Short-echo time single-voxel MRS (109) and  $^1\text{H}$ -MRS (110) have also demonstrated utility in differentiating primary brain tumors from brain metastasis. Although these *in vivo* imaging techniques show potential for the diagnosis and grading of tumors, histologic examination is still considered the gold standard.

#### Characterizing tumor cell density and microenvironment

Diffusion, DSC-, and DCE-MRI have been used to characterize the tumor microenvironment, including identifying areas of increased tumor cell density. Many authors have reported that areas of restricted diffusion due to increased cell density can be seen as areas of low ADC (111–112) and have demonstrated good correlation between cell density obtained using stereotactic biopsies and ADC values (94). From DCE-MRI, the  $v_e$  parameter, an estimate of the fractional extracellular extravascular space has also shown to be related to the



tumor cellularity (113, 114). Being able to track tumor cell density over time is critically important to understanding tumor growth in response to any treatment. In particular, in the setting of antiangiogenic therapy where tumors might "hide" behind a restored BBB, having a tool that reflects tumor cell density, and growth would be very useful (8). Unfortunately, disambiguating the components of the tumor microenvironment,—e.g., native brain tissue, gliosis from prior chemotherapy/radiation, infiltrating glioma cells, and peritumoral edema—has been challenging to accomplish with current MRI techniques.

### Tumor growth models

Tumor growth has been modeled using the reaction diffusion approach, which comprises both a diffusion component (lateral spread of the tumor cells) and a proliferation component (increase in tumor cell density; refs. 115–121). Using standard structural images such as T1-weighted and FLAIR or T2-weighted images to look at the enhancing portion of the tumor and the edema respectively, predictive models for the spread of the tumor in the brain have been created. These models use images acquired longitudinally over periods of days or months (with known intervals between acquisitions) and consider the different diffusion rates in white (higher) and gray matter (lower) and physical boundaries imposed by "impregnable" structures such as ventricles or dura. The use of these growth models in radiotherapy planning facilitates the creation of treatment plans that do not use uniform margins, but rather margins that are more likely an indication of the patterns of tumor spread, thus minimizing radiation to healthy tissue and optimizing radiation to tumor tissues (122). As more is learned about the complexity of the tumor microenvironment and molecular profiles of tumors, these models based on multiparametric MR are expected to become more sophisticated and their use in adaptive radiotherapy will perhaps become more routine.

### Tumor molecular profiles

MRI with contrast is the best tool to initially suggest the diagnosis of a brain tumor but surgery is needed to confirm the type of tumor. Molecular characterization of gliomas has advanced significantly in the past few years, and while imaging has lagged a bit in detecting these molecular alterations, early data suggest that MRI-based imaging features may be associated with certain genotypes. In particular, detection of IDH mutations and EGFR amplification seem the most promising.

**IDH-mutant tumors.** Mutations of the IDH metabolic enzymes (IDH1 and IDH2) have been found in more than 80% of grade II–III gliomas and secondary GBMs (33, 123), but very infrequently (<10%) in primary GBMs (124, 125), leading some researchers to suggest that gliomas with IDH mutations are a different subtype of tumor. GBM patients with IDH mutations typically have good prognosis with a 2- to 4-fold longer median survival compared with patients with wild-type IDH1 (126). On the other hand, IDH mutation seems to be an early oncogenic event that may switch cellular metabolism towards tumor formation. Thus, the ability to detect these

mutations *in vivo* could have an impact on the therapeutic choices for patients and for drug development targeting this pathway.

IDH mutations result in elevated levels of the "oncometabolite," D-2HG in the range of 5 to 35 mmol/L (127). These 2HG levels can be measured by MRS *in vivo* as seen in Fig. 6 (128). By comparison, D-2HG levels in tumors with wild-type IDH or in healthy tissue are several orders (2–3) of magnitude lower, and cannot be detected by MRS. Hence, 2HG may be an ideal imaging biomarker of the IDH mutation. However, reliable measurements of 2HG by MRS are challenging due to the spectral overlap of 2HG with other abundant brain metabolites such as glutamate, glutamine, phosphocreatine, and myoinositol. A variety of sequences and analysis techniques have been proposed. Recently, an optimized long-echo time MRS sequence has been shown to detect 2HG *in vivo* (129). Other techniques such as difference spectral editing and two-dimensional correlation spectroscopy (COSY) have been demonstrated to disambiguate 2HG detection in patients with mutant IDH glioma (130).

Accurate measurement of 2HG would be the first tumor-specific imaging marker rather than a surrogate marker. Although potentially useful biomarkers, contrast-enhanced MRI, water diffusion (DWI), edema (FLAIR), or other metabolites (choline MRS), are all surrogate markers of tumor-induced changes in vascular or are confounded by other physical changes that affect the interpretation of the MRI changes (e.g., gliosis in FLAIR). Being able to directly measure tumor burden has significant implications for drug development and response assessment.

### Epidermal growth factor receptor–amplified tumors.

Epidermal growth factor receptor (EGFR) amplification occurs in approximately 40% of GBMs and is an interesting therapeutic target with several EGFR inhibitors in clinical trials (131). Increased contrast-to-necrosis ratio (132), as well as restricted water diffusion, is correlated with EGFR amplification (133). In GBMs expressing the EGFR variant III (EGFRvIII) mutation, rCBV was increased compared with those not expressing the vIII mutation. In addition, an association was found between EGFR amplification and stable or decreased tumor perfusion during chemoradiation (24). Given the concern that EGFR amplification may be a poor prognostic feature, the cooccurrence with stable or decreased tumor perfusion is not surprising as stable or decreased tumor perfusion was also associated with worse prognosis.

Being able to detect EGFR amplification is clinically useful as more drugs targeting this pathway are developed. Knowing a patient may be eligible for an EGFR-targeting drug can help optimize therapy in individual patients and shed light on relapse patterns if there is loss of the imaging surrogate for EGFR amplification. It remains unclear, though, what actual physical property is being reflected on MRI in EGFR-amplified tumors or if these are imaging markers of increased tumor malignancy.

### Gauging tumor response to treatment

**Tumor response criteria (RANO/Macdonald).** MRI is critical to assessing tumor response to therapy and several response criteria have been proposed that measure the change

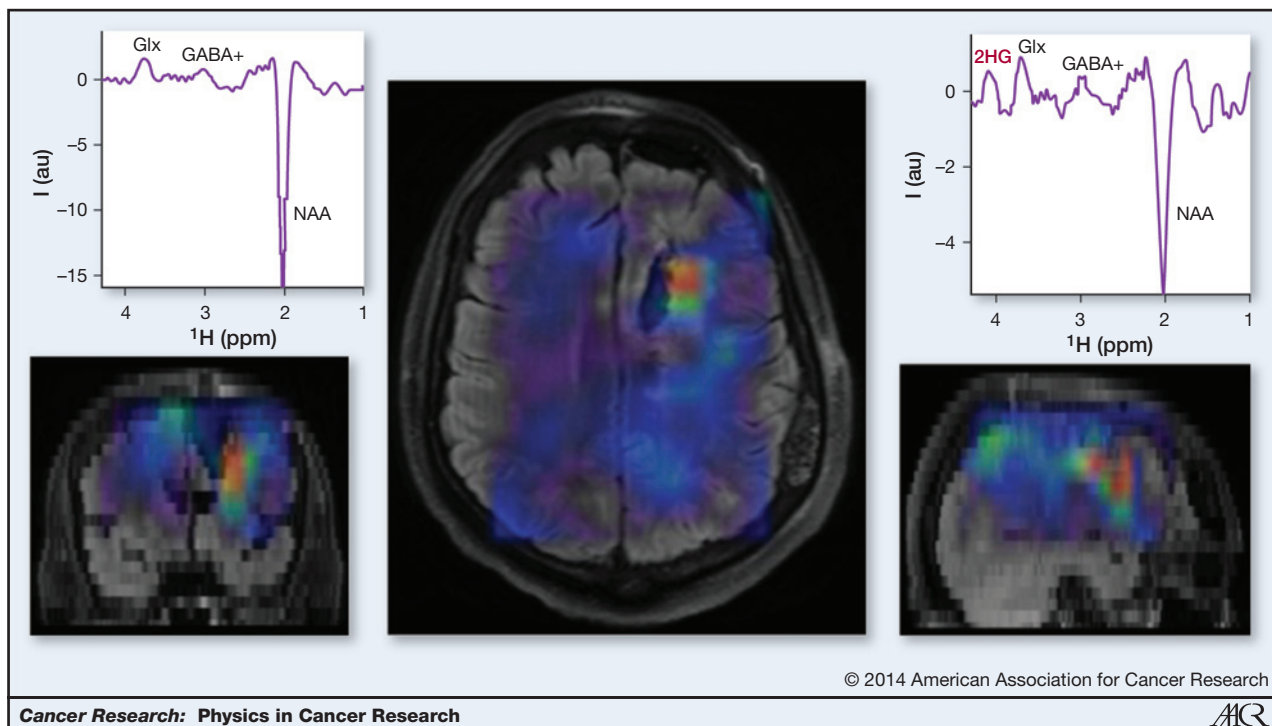


Figure 6. 3D imaging of 2HG in a glioma patient with IDH1 mutation. The 2HG map is overlaid on FLAIR anatomic imaging. High 2HG is found in a limited region around the postsurgical cavity. Note that edema in FLAIR image extends beyond the high 2HG area. Examples of difference of MEGA-LASER (121) edited spectra from a voxel in a tumor (right) and a voxel in the contralateral hemisphere are shown.

in the maximal area of contrast-enhancing tumor over time (9, 134). However, measuring the change in tumor diameter is crude for such a complex tumor and may not accurately reflect physical tumor responses to novel therapies, particularly those that are highly targeted or cytostatic. Therefore, there is a great deal of interest in incorporating in these response criteria some of the more sophisticated tools described below to better inform us about the biologic and physical changes occurring in tumors. The challenge is creating standardized techniques that can be easily implemented in a busy clinical workflow.

**Parametric response maps.** Functional diffusion maps (fDM; refs. 21, 135, 136) are a technique used to calculate changes in ADC on a voxel-by-voxel basis over time. Images acquired at different time points are registered and color-coded on the basis of the direction and magnitude of change. Stratification based on these maps (135, 137) has shown prognostic value in identifying outcomes in patients with high-grade glioma. The challenge with fDM is ensuring accurate longitudinal registration, particularly in the setting of large brain shifts that can happen with steroids or antiangiogenic therapy (136). Similar approaches with other MR-based parameters such as rCBV or Ktrans can also be used to track tumor response over time (138–140). These parametric maps are intuitively appealing because they may capture the underlying heterogeneity of GBM but technical challenges, such as the ability to accurately track voxels over time (registration), especially in the presence of changing tumors and resection cavities, have limited their widespread adoption.

**Monitoring tumor response to therapy—vascular normalization.** Clearly, accurate determination of tumor response/failure is critical for patient care and drug development. Unfortunately, the MacDonald and RANO response criteria (9, 10), which are based on more standard sequences (e.g., T1-weighted for MacDonald and T2/FLAIR for RANO), have significant limitations, leading to increased interest in modalities outside of routine anatomic sequences.

Given the hallmark of abnormal tumor vascularity, targeting tumor blood vessels is a principal therapy for high-grade gliomas. Both DSC and DCE-MRI have been used to characterize changes in the tumor vasculature in response to therapy. Early decrease in Ktrans, seen as soon as 1 day after the start of antiangiogenic therapy, has been associated with improved survival (25, 27). Results from two recent trials of antiangiogenic therapy, originally reported in recurrent GBM and confirmed in newly diagnosed GBM, have suggested that patients whose tumors showed improved perfusion after therapy had longer survival than patients who saw a drop in perfusion. In particular, there seems to be a window of vascular normalization during which radiation and chemotherapy may be more effective (24, 25, 27, 29, 94). Accurate imaging recognition of this window would be incredibly helpful in optimizing therapy for patients with glioma by concentrating chemotherapy or radiation to critical time periods and minimizing exposure to toxicity when they are least helpful.

Given the heterogeneity of tumor vasculature, vessel size MRI is an important tool for monitoring response to antiangiogenic therapies (24). A recent extension to the vessel size

approach, coined as vessel architecture imaging (VAI), exploits a temporal shift between the gradient and spin echo signals in DSC MRI and provides additional information about the microcirculation and tissue oxygenation status (141–143). Batchelor and colleagues demonstrated that antiangiogenic therapy improves microcirculation and normalizes oxygen saturation in patients with newly diagnosed and recurrent glioblastomas (24, 25). Furthermore, patients with these responses, suggesting vascular normalization, showed improved survival, so VAI has the potential to identify patients who would benefit from antiangiogenic therapies. Importantly, these changes in VAI and perfusion imaging occurred within 1 day of starting treatment and, thus, may serve as early biomarkers of response.

### Differentiating recurrent tumor from pseudoprogression and radiation necrosis

One of the biggest challenges in neuro-oncology clinical practice is the differentiation of treatment-related changes (particularly from radiation) and true tumor progression (144–146). Pseudoprogression and radiation necrosis reflect a spectrum of early to late changes represented by an increase in contrast enhancement due to blood vessel inflammation that can be misinterpreted as progressive tumor (147–149). In glioma patients treated with both radio- and chemotherapy, as many as 30% of patients experience pseudoprogression within the first 3 months of radiation (150–153). Clearly, distinguishing pseudoprogression from true tumor progression is critical to appropriate patient management as well as clinical trial enrollment. This is especially important with the advent of antiangiogenic therapy where administration of VEGF inhibitors during chemoradiation may modify the expression of pseudoprogression by imaging (144).

Conventional MRI findings cannot accurately distinguish between radiation damage and true progression because of similar appearances on postcontrast MRI. Physiologic imaging with DSC or DCE-MRI has returned mixed results. In small studies, DSC has been reported to aid in the discrimination between recurrence and radiation necrosis with elevated rCBV associated with tumor and low rCBV associated with necrosis (145, 154, 155). Low ADC values on DWI may also be suggestive of tumor (145). Higher Cho/Cr and Cho/NAA ratios on MRS have been reported in cases of tumor recurrence compared with the ratios seen for treatment-related changes (156, 157). Unfortunately, no single imaging technique is perfect and likely a combination of sequences will be needed to clarify this clinical dilemma. The lack of a gold standard to define treatment-related changes from active tumor—pathology samples often show various mixes of treatment-related changes and tumor—has hindered development of an MRI surrogate marker (9).

### Challenges and Opportunities

Although the use of MR imaging continues to enhance our understanding of the physical processes underlying glioma behavior, there are a number of challenges and opportunities for further research.

### Diffusion imaging

In DW-MRI, the relationship between ADC values and tumor cell density can be complex. Within a specific region of interest, areas of edema and necrosis can increase ADC, which can offset the effects of reduced ADC due to increased cell density. In addition, the impact that scarring and gliosis from chemotherapy or radiation have on ADC is unclear. Hypoxia is also reflected by low ADC values (as seen in ischemic stroke or after surgery); so, variation in tumor hypoxia may influence tumor ADC values. This is a particular challenge in the setting of antiangiogenic agents where there may be heterogeneous tumor responses: depending on dose and duration of therapy, vascular normalization, or vessel pruning may predominate. Although restricted diffusion lesions can be precursors to the appearance of contrast enhancement and tumor recurrence (8, 158), some such areas of restricted diffusion are potentially areas of tumor hypoxia and are seen in patients responding to antiangiogenic therapy (159).

More advanced diffusion imaging, including diffusion kurtosis imaging (DKI; ref. 160), high *b* value imaging, and restriction spectrum imaging (RSI) have sought to further elucidate the relationship between diffusion imaging and tumor cellularity (161, 162). In biologic tissues, two modes of diffusion have been proposed: restricted diffusion where the molecule is trapped within compartments (e.g., intraaxonal diffusion) and hindered diffusion where the diffusion is around obstructions (e.g., extra-axonal diffusion; ref. 163). ADC reflects both hindered and restricted diffusion pools within a voxel; thus, this value cannot tease out the distinction between these microstructural differences.

The more routinely acquired DTI used to calculate ADC assumes a Gaussian behavior in calculating the diffusion tensor, which is not strictly true in tissues where diffusion is restricted. This deviation from Gaussian diffusion behavior can be studied using DKI by means of the apparent excess kurtosis coefficient (160, 164). DKI requires additional gradient directions (at least 15) to estimate the tensor and has demonstrated success in grading tumors (160).

There are concerns that the often-profound reductions in the contrast enhancement and leakage observed immediately after the start of antiangiogenic therapy may reflect a normalization of vascular rather than a true antitumor effect ("pseudoresponse"; ref. 93). White and colleagues proposed that RSI (165) allows for the separation of the hindered and restricted diffusion components. This can be especially relevant in the context of antiangiogenic therapies where contrast enhancement and FLAIR hyperintensity can change significantly without corresponding changes in tumor response. As shown by Kothari and colleagues (161), RSI-based cellularity maps are more robust than standard ADC in identifying areas of tumor in patients treated with antiangiogenic therapies. By suppressing the signal arising from the hindered diffusion in the edema while increasing the sensitivity to the restricted diffusion in the tumor cells, RSI is shown to improve tumor conspicuity (161) and to be less sensitive to treatment-induced changes in areas of FLAIR hyperintensity.

Thus, a variety of diffusion models are being studied with a goal of being able to shed further light on the tumor microstructure (166).



## DCE-MRI

Various studies have indicated that the Tofts models for DCE imaging may be inadequate in the case of non-well-mixed spaces (heterogeneous tissues) and in necrotic regions, which both naturally occur in tumor tissue (167–169). One limitation is that these models are based on the assumptions of instantly well-mixed interstitial spaces and effectively infinitely fast transcytolemmal water exchange, which is not realistic in tumor. Further refinements to the model, the so-called "shutter-speed" (170) model, allow for finite transcytolemmal water molecule exchange kinetics and have the potential to better discriminate benign from malignant lesions and are being used to monitor early response to therapy. Numerous studies have also failed to establish a strong relationship between  $v_e$ , the DCE-based biomarker of tissue cellularity and tumor cellularity as seen in histology (171). In addition, Mills and colleagues observed a lack of hypothesized relationship between the ADC obtained from diffusion imaging and  $v_e$ , although both measures are believed to be indicators of the tumor cellularity (172). More work needs to be done to model the true exchange of contrast across tumor vascular walls and diffusion through interstitial spaces. Using phantoms and computer models as well as direct comparison to tumor tissue will be critical to refine these models and improve our understanding of what the calculated parameters are actually measuring. Capturing the full signal–time curve from contrast extravasation to wash out requires many minutes of scanning and so is subject to patient motion. This has prompted investigation of faster acquisition techniques or forced tradeoffs between temporal and spatial resolution.

## DSC-MRI

Similar challenges are seen in the use of DSC in the study of GBMs. For example, although rCBV, as measured using DSC-MRI is elevated in tumors, reported correlations between rCBV and glioma grades are challenged by overlap in rCBV values across grades (101). In brain tumors, due to disruptions in the BBB, the loss of signal intensity due to contrast susceptibility

effects in blood vessels can be offset by signal intensity increases in surrounding tissue due to T1 effects arising from the extravasation of the CA (101). The difference in susceptibility between the blood vessels and the surrounding tissue is lessened, leading to underestimation in the rCBV, and may account for some of the mixed results in using rCBV as a biomarker for tumor grade. Correction of these effects has led to a better correlation between rCBV and tumor grade. Similarly, the use of a "pre-load" of CA to saturate the tissue space and, thus, reduce the T1 effects is now recommended (173).

In conclusion, using physical principles, advanced MR imaging provides insights into physical and biologic processes in GBM, a deadly disease with a dismal prognosis. MR-based biomarkers are being developed and validated in the diagnosis and assessment of response to therapy in patients with glioblastoma. Despite these technical advances, noninvasive MR has yet to demonstrate the diagnostic accuracy necessary to replace biopsies in the diagnosis and grading of gliomas, the differentiation of tumor recurrence from radiation necrosis, and to accurately measure tumor cellularity and extent. However, recent advances such as vessel architecture imaging, restricted spectrum imaging, sophisticated models for the analysis of DCE-MRI, and the use of MRS for the detection of IDH mutations *in vivo* offer promise that we might get there in the near future.

## Disclosure of Potential Conflicts of Interest

K.E. Emblem has provided expert testimony for intellectual property rights, NordicNeuroLab AS, Bergen, Norway. No potential conflicts of interest were disclosed by the other authors.

## Grant Support

J. Kalpathy-Cramer is funded in part by the NIH grants U01CA154602 and R00LM009889, E.R. Gerstner is supported in part by NIH grant U01CA154602, K.E. Emblem is funded by South-Eastern Norway Regional Health Authority Grant 2013069, O. Andronesi is funded in part by a K22 Career Development Award from the National Cancer Institute of the NIH (K22CA178269-01) and B. Rosen is funded in part by NCI/NIH grant U01CA154602.

Received February 8, 2014; revised February 20, 2014; accepted May 19, 2014; published online September 2, 2014.

## References

- Stupp R, Hegi ME, Mason WP, van den Bent MJ, Taphoorn MJ, Janzer RC, et al. Effects of radiotherapy with concomitant and adjuvant temozolomide versus radiotherapy alone on survival in glioblastoma in a randomised phase III study: 5-year analysis of the EORTC-NCIC trial. *Lancet Oncol* 2009;10:459–66.
- Grossman SA, Ye X, Piantadosi S, Desideri S, Nabors LB, Rosenfeld M, et al. Survival of patients with newly diagnosed glioblastoma treated with radiation and temozolomide in research studies in the United States. *Clin Cancer Res* 2010;16:2443–9.
- Lai A, Tran A, Nghiemphu PL, Pope WB, Solis OE, Selch M, et al. Phase II study of bevacizumab plus temozolomide during and after radiation therapy for patients with newly diagnosed glioblastoma multiforme. *J Clin Oncol* 2011;29:142–8.
- Dolecek TA, Propp JM, Stroup NE, Kruchko C. CBTRUS statistical report: primary brain and central nervous system tumors diagnosed in the United States in 2005–2009. *Neuro Oncol* 2012;14 Suppl 5:v1–49.
- Wen PY, Kesari S. Malignant gliomas in adults. *N Engl J Med* 2008;359:492–507.
- Al-Okaili RN, Krejza J, Wang S, Woo JH, Melhem ER. Advanced MR imaging techniques in the diagnosis of intraaxial brain tumors in adults. *Radiographics* 2006;26 Suppl 1:S173–89.
- Pope WB, Sayre J, Perlina A, Villablanca JP, Mischel PS, Cloughesy TF. MR imaging correlates of survival in patients with high-grade gliomas. *AJNR Am J Neuroradiol* 2005;26:2466–74.
- Gerstner ER, Chen PJ, Wen PY, Jain RK, Batchelor TT, Sorensen G. Infiltrative patterns of glioblastoma spread detected via diffusion MRI after treatment with cediranib. *Neuro Oncol* 2010;12:466–72.
- Wen PY, Macdonald DR, Reardon DA, Cloughesy TF, Sorensen AG, Galanis E, et al. Updated response assessment criteria for high-grade gliomas: response assessment in neuro-oncology working group. *J Clin Oncol* 2010;28:1963–72.
- Chinot OL, Macdonald DR, Abrey LE, Zahlmann G, Kerloeguen Y, Cloughesy TF. Response assessment criteria for glioblastoma: practical adaptation and implementation in clinical trials of antiangiogenic therapy. *Curr Neurol Neurosci Rep* 2013;13:347.
- Jain RK, di Tomaso E, Duda DG, Loeffler JS, Sorensen AG, Batchelor TT. Angiogenesis in brain tumours. *Nat Rev Neurosci* 2007;8:610–22.
- Pries AR, Hopfner M, le Noble F, Dewhirst MW, Secomb TW. The shunt problem: control of functional shunting in normal and tumour vasculature. *Nat Rev Cancer* 2010;10:587–93.
- Jain RK. Normalizing tumor microenvironment to treat cancer: bench to bedside to biomarkers. *J Clin Oncol* 2013;31:2205–18.

14. Guo P, Hu B, Gu W, Xu L, Wang D, Huang HJ, et al. Platelet-derived growth factor-B enhances glioma angiogenesis by stimulating vascular endothelial growth factor expression in tumor endothelia and by promoting pericyte recruitment. *Am J Pathol* 2003;162:1083–93.
15. Svolos P, Tsolaki E, Kapsalaki E, Theodorou K, Fountas K, Fezoulidis I, et al. Investigating brain tumor differentiation with diffusion and perfusion metrics at 3T MRI using pattern recognition techniques. *Magn Reson Imaging* 2013;31:1567–77.
16. Young GS. Advanced MRI of adult brain tumors. *Neurol Clin* 2007;25:947–73.
17. Jain R, Griffith B, Narang J, Mikkelsen T, Bagher-Ebadian H, Nejad-Davarani SP, et al. Blood-brain-barrier imaging in brain tumors: concepts and methods. *Neurographics* 2012;2:48–59.
18. Ellingson BM, Cloughesy TF, Lai A, Nghiemphu PL, Pope WB. Cell invasion, motility, and proliferation level estimate (CIMPLE) maps derived from serial diffusion MR images in recurrent glioblastoma treated with bevacizumab. *J Neurooncol* 2011;105:91–101.
19. Gerstner ER, Sorensen AG. Diffusion and diffusion tensor imaging in brain cancer. *Semin Radiat Oncol* 2011;21:141–6.
20. Farrar CT, Kamoun WS, Ley CD, Kim YR, Kwon SJ, Dai G, et al. *In vivo* validation of MRI vessel caliber index measurement methods with intravital optical microscopy in a U87 mouse brain tumor model. *Neuro Oncol* 2010;12:341–50.
21. Hamstra DA, Rehemtulla A, Ross BD. Diffusion magnetic resonance imaging: a biomarker for treatment response in oncology. *J Clin Oncol* 2007;25:4104–9.
22. Chenevert TL, Stegman LD, Taylor JM, Robertson PL, Greenberg HS, Rehemtulla A, et al. Diffusion magnetic resonance imaging: an early surrogate marker of therapeutic efficacy in brain tumors. *J Natl Cancer Inst* 2000;92:2029–36.
23. Provenzale JM, Mukundan S, Barboriak DP. Diffusion-weighted and perfusion MR imaging for brain tumor characterization and assessment of treatment response. *Radiology* 2006;239:632–49.
24. Batchelor TT, Gerstner ER, Emblem KE, Duda DG, Kalpathy-Cramer J, Snuderl M, et al. Improved tumor oxygenation and survival in glioblastoma patients who show increased blood perfusion after cediranib and chemoradiation. *Proc Natl Acad Sci U S A* 2013;110:19059–64.
25. Sorensen AG, Batchelor TT, Zhang WT, Chen PJ, Yeo P, Wang M, et al. A "vascular normalization index" as potential mechanistic biomarker to predict survival after a single dose of cediranib in recurrent glioblastoma patients. *Cancer Res* 2009;69:5296–300.
26. Jain RK. Normalization of tumor vasculature: an emerging concept in antiangiogenic therapy. *Science* 2005;307:58–62.
27. Sorensen AG, Emblem KE, Polaskova P, Jennings D, Kim H, Ancukiewicz M, et al. Increased survival of glioblastoma patients who respond to antiangiogenic therapy with elevated blood perfusion. *Cancer Res* 2012;72:402–7.
28. Goel S, Duda DG, Xu L, Munn LL, Boucher Y, Fukumura D, et al. Normalization of the vasculature for treatment of cancer and other diseases. *Physiol Rev* 2011;91:1071–121.
29. Batchelor TT, Sorensen AG, di Tomaso E, Zhang WT, Duda DG, Cohen KS, et al. AZD2171, a pan-VEGF receptor tyrosine kinase inhibitor, normalizes tumor vasculature and alleviates edema in glioblastoma patients. *Cancer Cell* 2007;11:83–95.
30. Padhani AR, Leach MO. Antivascular cancer treatments: functional assessments by dynamic contrast-enhanced magnetic resonance imaging. *Abdom Imaging* 2005;30:324–41.
31. Emblem KE, Zoellner FG, Tennoe B, Nedregaard B, Nome T, Due-Tonnessen P, et al. Predictive modeling in glioma grading from MR perfusion images using support vector machines. *Magn Reson Med* 2008;60:945–52.
32. Padhani AR, Miles KA. Multiparametric imaging of tumor response to therapy. *Radiology* 2010;256:348–64.
33. Yan H, Parsons DW, Jin G, McLendon R, Rasheed BA, Yuan W, et al. IDH1 and IDH2 mutations in gliomas. *N Engl J Med* 2009;360:765–73.
34. Lee EQ, Kuhn J, Lamborn KR, Abrey L, DeAngelis LM, Lieberman F, et al. Phase I/II study of sorafenib in combination with temsirolimus for recurrent glioblastoma or gliosarcoma: North American Brain Tumor Consortium study 05-02. *Neuro Oncol* 2012;14:1511–8.
35. Peereboom DM, Ahluwalia MS, Ye X, Supko JG, Hilderbrand SL, Phuphanich S, et al. NABTT 0502: a phase II and pharmacokinetic study of erlotinib and sorafenib for patients with progressive or recurrent glioblastoma multiforme. *Neuro Oncol* 2013;15:490–6.
36. Batchelor TT, Mulholland P, Neyns B, Nabors LB, Campone M, Wick A, et al. Phase III randomized trial comparing the efficacy of cediranib as monotherapy, and in combination with lomustine, versus lomustine alone in patients with recurrent glioblastoma. *J Clin Oncol* 2013;31:3212–8.
37. Parker GJM, Padhani AR. *T<sub>1</sub>-W DCE-MRI: T<sub>1</sub>-Weighted Dynamic Contrast-Enhanced MRI*. In: Tofts P, editor. *Quantitative MRI of the Brain*. Chichester, UK: John Wiley & Sons, Ltd; 2003.
38. Stevenson VL, Parker GJ, Barker GJ, Birnie K, Tofts PS, Miller DH, et al. Variations in T1 and T2 relaxation times of normal appearing white matter and lesions in multiple sclerosis. *J Neurol Sci* 2000;178:81–7.
39. Jain RK, Booth MF. What brings pericytes to tumor vessels? *J Clin Invest* 2003;112:1134–6.
40. Tofts PS, Brix G, Buckley DL, Evelhoch JL, Henderson E, Knopp MV, et al. Estimating kinetic parameters from dynamic contrast-enhanced T(1)-weighted MRI of a diffusible tracer: standardized quantities and symbols. *J Magn Reson Imaging* 1999;10:223–32.
41. Parker GJ, Tofts PS. Pharmacokinetic analysis of neoplasms using contrast-enhanced dynamic magnetic resonance imaging. *Top Magn Reson Imaging* 1999;10:130–42.
42. Jackson A. Imaging microvascular structure with contrast enhanced MRI. *Br J Radiol* 2003;76:S159–73.
43. Harrer JU, Parker GJ, Haroon HA, Buckley DL, Emberton K, Roberts C, et al. Comparative study of methods for determining vascular permeability and blood volume in human gliomas. *J Magn Reson Imaging* 2004;20:748–57.
44. Jackson A. Analysis of dynamic contrast enhanced MRI. *Br J Radiol* 2004;77 Spec No 2:S154–66.
45. Collins DJ, Padhani AR. Dynamic magnetic resonance imaging of tumor perfusion. Approaches and biomedical challenges. *IEEE Eng Med Biol Mag* 2004;23:65–83.
46. Roberts C, Issa B, Stone A, Jackson A, Waterton JC, Parker GJ. Comparative study into the robustness of compartmental modeling and model-free analysis in DCE-MRI studies. *J Magn Reson Imaging* 2006;23:554–63.
47. Jackson A, O'Connor JP, Parker GJ, Jayson GC. Imaging tumor vascular heterogeneity and angiogenesis using dynamic contrast-enhanced magnetic resonance imaging. *Clin Cancer Res* 2007;13:3449–59.
48. O'Connor JP, Jackson A, Asselin MC, Buckley DL, Parker GJ, Jayson GC. Quantitative imaging biomarkers in the clinical development of targeted therapeutics: current and future perspectives. *Lancet Oncol* 2008;9:766–76.
49. Barboriak DP, MacFall JR, Viglianti BL, Dewhirst Dvm MW. Comparison of three physiologically-based pharmacokinetic models for the prediction of contrast agent distribution measured by dynamic MR imaging. *J Magn Reson Imaging* 2008;27:1388–98.
50. Patlak CS, Blasberg RG, Fenstermacher JD. Graphical evaluation of blood-to-brain transfer constants from multiple-time uptake data. *J Cereb Blood Flow Metab* 1983;3:1–7.
51. Ferl GZ, Xu L, Friesenhahn M, Bernstein LJ, Barboriak DP, Port RE. An automated method for nonparametric kinetic analysis of clinical DCE-MRI data: application to glioblastoma treated with bevacizumab. *Magn Reson Med* 2010;63:1366–75.
52. Parker GJM, Suckling J, Tanner SF, Padhani AR, Revell PB, Husband JE, et al. Probing tumor microvasculature by measurement, analysis and display of contrast agent uptake kinetics. *J Magn Reson Imaging* 1997;7:564–74.
53. Tofts PS. Modeling tracer kinetics in dynamic Gd-DTPA MR imaging. *J Magn Reson Imaging* 1997;7:91–101.
54. Sourbron SP, Buckley DL. On the scope and interpretation of the Tofts models for DCE-MRI. *Magn Reson Med* 2011;66:735–45.
55. Schenck JF. The role of magnetic susceptibility in magnetic resonance imaging: MRI magnetic compatibility of the first and second kinds. *Med Phys* 1996;23:815–50.

56. Rosen BR, Belliveau JW, Vevea JM, Brady TJ. Perfusion imaging with NMR contrast agents. *Magn Reson Med* 1990;14:249–65.
57. Belliveau JW, Rosen BR, Kantor HL, Rzedzian RR, Kennedy DN, McKinstry RC, et al. Functional cerebral imaging by susceptibility-contrast NMR. *Magn Reson Med* 1990;14:538–46.
58. Rosen BR, Belliveau JW, Aronen HJ, Kennedy D, Buchbinder BR, Fischman A, et al. Susceptibility contrast imaging of cerebral blood volume: human experience. *Magn Reson Med* 1991;22:293–9.
59. Meier P, Zierler KL. On the theory of the indicator-dilution method for measurement of blood flow and volume. *J Appl Physiol* 1954;6:731–44.
60. Zaharchuk G. Theoretical basis of hemodynamic MR imaging techniques to measure cerebral blood volume, cerebral blood flow, and permeability. *AJNR Am J Neuroradiol* 2007;28:1850–8.
61. Ostergaard L, Weisskoff RM, Chesler DA, Gyldensted C, Rosen BR. High resolution measurement of cerebral blood flow using intravascular tracer bolus passages. Part I: Mathematical approach and statistical analysis. *Magn Reson Med* 1996;36:715–25.
62. Cha S, Knopp EA, Johnson G, Wetzel SG, Litt AW, Zagzag D. Intracranial mass lesions: dynamic contrast-enhanced susceptibility-weighted echo-planar perfusion MR imaging. *Radiology* 2002; 223:11–29.
63. van Osch MJ, Vonken EJ, Bakker CJ, Viergever MA. Correcting partial volume artifacts of the arterial input function in quantitative cerebral perfusion MRI. *Magn Reson Med* 2001;45:477–85.
64. Fisel CR, Ackerman JL, Buxton RB, Garrido L, Belliveau JW, Rosen BR, et al. MR contrast due to microscopically heterogeneous magnetic susceptibility: numerical simulations and applications to cerebral physiology. *Magn Reson Med* 1991;17:336–47.
65. Rosen BR, Belliveau JW, Buchbinder BR, McKinstry RC, Porkka LM, Kennedy DN, et al. Contrast agents and cerebral hemodynamics. *Magn Reson Med* 1991;19:285–92.
66. Weisskoff RM, Zuo CS, Boxerman JL, Rosen BR. Microscopic susceptibility variation and transverse relaxation: theory and experiment. *Magn Reson Med* 1994;31:601–10.
67. Boxerman JL, Hamberg LM, Rosen BR, Weisskoff RM. MR contrast due to intravascular magnetic susceptibility perturbations. *Magn Reson Med* 1995;34:555–66.
68. Dennie J, Mandeville JB, Boxerman JL, Packard SD, Rosen BR, Weisskoff RM. NMR imaging of changes in vascular morphology due to tumor angiogenesis. *Magn Reson Med* 1998;40:793–9.
69. Einstein A. [Über die von der molekularkinetischen Theorie der Wärme geforderte Bewegung von in ruhenden Flüssigkeiten suspendierten Teilchen]. *Annalen der Physik* 1905;322:549–60.
70. Le Bihan D, Mangin JF, Poupon C, Clark CA, Pappata S, Molko N, et al. Diffusion tensor imaging: concepts and applications. *J Magn Reson Imaging* 2001;13:534–46.
71. Hagmann P, Jonasson L, Maeder P, Thiran J-P, Wedeen VJ, Meuli R. Understanding diffusion MR imaging techniques: from scalar diffusion-weighted imaging to diffusion tensor imaging and beyond. *Radiographics* 2006;26:S205–23.
72. Le Bihan D, Johansen-Berg H. Diffusion MRI at 25: exploring brain tissue structure and function. *Neuroimage* 2012;61:324–41.
73. Chenevert T, McKeever P, Ross B. Monitoring early response of experimental brain tumors to therapy using diffusion magnetic resonance imaging. *Clin Cancer Res* 1997;3:1457–66.
74. Chenevert TL, Ross BD. Diffusion imaging for therapy response assessment of brain tumor. *Neuroimaging Clin N Am* 2009;19:559–71.
75. Chenevert TL, Sundgren PC, Ross BD. Diffusion imaging: insight to cell status and cytoarchitecture. *Neuroimaging Clin N Am* 2006; 16:619–32, viii–ix.
76. Negendank W. Studies of human tumors by MRS: a review. *NMR Biomed* 1992;5:303–24.
77. Kauppinen RA, Peet AC. Using magnetic resonance imaging and spectroscopy in cancer diagnostics and monitoring preclinical and clinical approaches. *Cancer Biol Ther* 2011;12:665–79.
78. Nelson SJ. Multivoxel magnetic resonance spectroscopy of brain tumors. *Mol Cancer Ther* 2003;2:497–507.
79. Bluml S, Moreno-Torres A, Shic F, Nguy CH, Ross BD. Tricarboxylic acid cycle of glia in the *in vivo* human brain. *NMR Biomed* 2002; 15:1–5.
80. Mora B, Narasimhan PT, Ross BD, Allman J, Barker PB.  $^{31}\text{P}$  saturation transfer and phosphocreatine imaging in the monkey brain. *Proc Natl Acad Sci U S A* 1991;88:8372–6.
81. Wijnen JP, Van der Graaf M, Scheenen TW, Klomp DW, de Galan BE, Idema AJ, et al. *In vivo*  $^{13}\text{C}$  magnetic resonance spectroscopy of a human brain tumor after application of  $^{13}\text{C}$ -1-enriched glucose. *Magn Reson Imaging* 2010;28:690–7.
82. Lanz B, Xin L, Millet P, Gruetter R. *In vivo* quantification of neuro-glial metabolism and glial glutamate concentration using (1) H-[(13) C] MRS at 14.1T. *J Neurochem* 2014;128:125–39.
83. Park JM, Josan S, Grafendorfer T, Yen YF, Hurd RE, Spielman DM, et al. Measuring mitochondrial metabolism in rat brain *in vivo* using MR Spectroscopy of hyperpolarized [2-(1)(3)C]pyruvate. *NMR Biomed* 2013;26:1197–203.
84. Bohndiek SE, Kettunen MI, Hu DE, Witney TH, Kennedy BW, Gallagher FA, et al. Detection of tumor response to a vascular disrupting agent by hyperpolarized  $^{13}\text{C}$  magnetic resonance spectroscopy. *Mol Cancer Ther* 2010;9:3278–88.
85. Park I, Larson PE, Zierhut ML, Hu S, Bok R, Ozawa T, et al. Hyperpolarized  $^{13}\text{C}$  magnetic resonance metabolic imaging: application to brain tumors. *Neuro Oncol* 2010;12:133–44.
86. Ward CS, Venkatesh HS, Chaumeil MM, Brandes AH, Vancracking M, Dafni H, et al. Noninvasive detection of target modulation following phosphatidylinositol 3-kinase inhibition using hyperpolarized  $^{13}\text{C}$  magnetic resonance spectroscopy. *Cancer Res* 2010;70:1296–305.
87. Warren WS, Jenista E, Branca RT, Chen X. Increasing hyperpolarized spin lifetimes through true singlet eigenstates. *Science* 2009; 323:1711–4.
88. Pileio G1, Bowen S, Laustsen C, Tayler MC, Hill-Cousins JT, Brown LJ, Brown RC, Ardenkjaer-Larsen JH, Levitt MH. Recycling and imaging of nuclear singlet hyperpolarization. *J Am Chem Soc* 2013; 135:5084–8.
89. Griffin JL, Shockcor JP. Metabolic profiles of cancer cells. *Nat Rev Cancer* 2004;4:551–61.
90. Dowling C, Bollen AW, Noworolski SM, McDermott MW, Barbaro NM, Day MR, et al. Preoperative proton MR spectroscopic imaging of brain tumors: correlation with histopathologic analysis of resection specimens. *Am J Neuroradiol* 2001;22:604–12.
91. Nelson SJ. Assessment of therapeutic response and treatment planning for brain tumors using metabolic and physiological MRI. *NMR Biomed* 2011;24:734–49.
92. Hamstra DA, Lee KC, Tychevicz JM, Schepkin VD, Moffat BA, Chen M, et al. The use of 19F spectroscopy and diffusion-weighted MRI to evaluate differences in gene-dependent enzyme prodrug therapies. *Mol Ther* 2004;10:916–28.
93. Clarke JL, Chang S. Pseudoprogression and pseudoresponse: challenges in brain tumor imaging. *Curr Neurol Neurosci Rep* 2009;9: 241–6.
94. Batchelor TT, Duda DG, di Tomaso E, Ancukiewicz M, Plotkin SR, Gerstner E, et al. Phase II study of cediranib, an oral pan-vascular endothelial growth factor receptor tyrosine kinase inhibitor, in patients with recurrent glioblastoma. *J Clin Oncol* 2010;28:2817–23.
95. Maia AC Jr, Malheiros SM, da Rocha AJ, Stavale JN, Guimaraes IF, Borges LR, et al. Stereotactic biopsy guidance in adults with supratentorial nonenhancing gliomas: role of perfusion-weighted magnetic resonance imaging. *J Neurosurg* 2004;101:970–6.
96. Lev MH, Ozsunar Y, Henson JW, Rasheed AA, Barest GD, Harsh GR, et al. Glioma tumor grading and outcome prediction using dynamic spin-echo MR susceptibility mapping compared with conventional contrast-enhanced MR: confounding effect of elevated rCBV of oligodendrogliomas. *AJNR Am J Neuroradiol* 2004;25:214–21.
97. Covarrubias DJ, Rosen BR, Lev MH. Dynamic magnetic resonance perfusion imaging of brain tumors. *Oncologist* 2004;9:528–37.
98. Law M, Yang S, Wang H, Babb JS, Johnson G, Cha S, et al. Glioma grading: sensitivity, specificity, and predictive values of perfusion MR imaging and proton MR spectroscopic imaging compared with conventional MR imaging. *AJNR Am J Neuroradiol* 2003;24: 1989–98.
99. Law M, Yang S, Babb JS, Knopp EA, Golfinos JG, Zagzag D, et al. Comparison of cerebral blood volume and vascular permeability from



- dynamic susceptibility contrast-enhanced perfusion MR imaging with glioma grade. *AJNR Am J Neuroradiol* 2004;25:746–55.
100. Law M, Young R, Babb J, Rad M, Sasaki T, Zagzag D, et al. Comparing perfusion metrics obtained from a single compartment versus pharmacokinetic modeling methods using dynamic susceptibility contrast-enhanced perfusion MR imaging with glioma grade. *AJNR Am J Neuroradiol* 2006;27:1975–82.
  101. Boxerman JL, Schmainda KM, Weisskoff RM. Relative cerebral blood volume maps corrected for contrast agent extravasation significantly correlate with glioma tumor grade, whereas uncorrected maps do not. *AJNR Am J Neuroradiol* 2006;27:859–67.
  102. Danchaivijitr N, Waldman AD, Tozer DJ, Benton CE, Brasil Caseiras G, Tofts PS, et al. Low-grade gliomas: do changes in rCBV measurements at longitudinal perfusion-weighted MR imaging predict malignant transformation? *Radiology* 2008;247:170–8.
  103. Ludemann L, Grieger W, Wurm R, Budzisch M, Hamm B, Zimmer C. Comparison of dynamic contrast-enhanced MRI with WHO tumor grading for gliomas. *Eur Radiol* 2001;11:1231–41.
  104. Awasthi R, Rathore RK, Soni P, Sahoo P, Awasthi A, Husain N, et al. Discriminant analysis to classify glioma grading using dynamic contrast-enhanced MRI and immunohistochemical markers. *Neuroradiology* 2012;54:205–13.
  105. Liu X, Tian W, Kolar B, Yeane GA, Qiu X, Johnson MD, et al. MR diffusion tensor and perfusion-weighted imaging in preoperative grading of supratentorial nonenhancing gliomas. *Neuro Oncol* 2011;13:447–55.
  106. Byrnes TJ, Barrick TR, Bell BA, Clark CA. Diffusion tensor imaging discriminates between glioblastoma and cerebral metastases *in vivo*. *NMR Biomed* 2011;24:54–60.
  107. Nimsy C, Ganslandt O, Hastreiter P, Wang R, Benner T, Sorensen AG, et al. Preoperative and intraoperative diffusion tensor imaging-based fiber tracking in glioma surgery. *Neurosurgery* 2007;61:178–85.
  108. Kekhia H, Rigolo L, Norton I, Golby AJ. Special surgical considerations for functional brain mapping. *Neurosurg Clin N Am* 2011;22:111–32, vii.
  109. Crisi G, Orsingher L, Filice S. Lipid and macromolecules quantitation in differentiating glioblastoma from solitary metastasis: a short-echo time single-voxel magnetic resonance spectroscopy study at 3 T. *J Comput Assist Tomogr* 2013;37:265–71.
  110. Tsougos I, Svolos P, Kousi E, Fountas K, Theodorou K, Fezoulidis I, et al. Differentiation of glioblastoma multiforme from metastatic brain tumor using proton magnetic resonance spectroscopy, diffusion and perfusion metrics at 3 T. *Cancer Imaging* 2012;12:423–36.
  111. Ellingson BM, Malkin MG, Rand SD, Connelly JM, Quinsey C, LaViola PS, et al. Validation of functional diffusion maps (fDMs) as a biomarker for human glioma cellularity. *J Magn Reson Imaging* 2010;31:538–48.
  112. Sugahara T, Korogi Y, Kochi M, Ikushima I, Shigematu Y, Hirai T, et al. Usefulness of diffusion-weighted MRI with echo-planar technique in the evaluation of cellularity in gliomas. *J Magn Reson Imaging* 1999;9:53–60.
  113. Aref M, Chaudhari AR, Bailey KL, Aref S, Wiener EC. Comparison of tumor histology to dynamic contrast enhanced magnetic resonance imaging-based physiological estimates. *Magn Reson Imaging* 2008;26:1279–93.
  114. Aryal MP, Nagaraja TN, Keenan KA, Bagher-Ebadian H, Panda S, Brown SL, et al. Dynamic contrast enhanced MRI parameters and tumor cellularity in a rat model of cerebral glioma at 7 T. *Magn Reson Med* 2014;71:2206–14.
  115. Swanson KR, Rostomily RC, Alvord EC Jr. A mathematical modelling tool for predicting survival of individual patients following resection of glioblastoma: a proof of principle. *Br J Cancer* 2008;98:113–9.
  116. Hawkins-Daarud A, Rockne RC, Anderson AR, Swanson KR. Modeling tumor-associated edema in gliomas during anti-angiogenic therapy and its impact on imageable tumor. *Front Oncol* 2013;3:66.
  117. Wang CH, Rockhill JK, Mrugala M, Peacock DL, Lai A, Jusenius K, et al. Prognostic significance of growth kinetics in newly diagnosed glioblastomas revealed by combining serial imaging with a novel biomathematical model. *Cancer Res* 2009;69:9133–40.
  118. Swanson KR, Rockne RC, Claridge J, Chaplain MA, Alvord EC Jr, Anderson AR. Quantifying the role of angiogenesis in malignant progression of gliomas: in silico modeling integrates imaging and histology. *Cancer Res* 2011;71:7366–75.
  119. Alvord EC, Swanson KR. Using mathematical modeling to predict survival of low-grade gliomas. *Ann Neurol* 2007;61:496.
  120. Swanson KR, Harpold HL, Peacock DL, Rockne R, Pennington C, Kilbride L, et al. Velocity of radial expansion of contrast-enhancing gliomas and the effectiveness of radiotherapy in individual patients: a proof of principle. *Clin Oncol* 2008;20:301–8.
  121. Swanson KR, Bridge C, Murray JD, Alvord J, Ellsworth C. Virtual and real brain tumors: using mathematical modeling to quantify glioma growth and invasion. *J Neurol Sci* 2003;216:1–10.
  122. Corwin D, Holdsworth C, Rockne RC, Trister AD, Mrugala MM, Rockhill JK, et al. Toward patient-specific, biologically optimized radiation therapy plans for the treatment of glioblastoma. *PLoS ONE* 2013;8:e79115.
  123. Zou P, Xu H, Chen P, Yan Q, Zhao L, Zhao P, et al. IDH1/IDH2 mutations define the prognosis and molecular profiles of patients with gliomas: a meta-analysis. *PLoS ONE* 2013;8:e68782.
  124. Cohen AL, Holmen SL, Colman H. IDH1 and IDH2 mutations in gliomas. *Curr Neurol Neurosci Rep* 2013;13:345.
  125. Weller M, Wick W, von Deimling A. Isocitrate dehydrogenase mutations: a challenge to traditional views on the genesis and malignant progression of gliomas. *Glia* 2011;59:1200–4.
  126. Houillier C, Wang X, Kaloshi G, Mokhtari K, Guillemin R, Laffaire J, et al. IDH1 or IDH2 mutations predict longer survival and response to temozolomide in low-grade gliomas. *Neurology* 2010;75:1560–6.
  127. Dang L, White DW, Gross S, Bennett BD, Bittiger MA, Driggers EM, et al. Cancer-associated IDH1 mutations produce 2-hydroxyglutamate. *Nature* 2010;465:966.
  128. Andronesi OC, Kim GS, Gerstner E, Batchelor T, Zika AA, Fantin VR, et al. Detection of 2-hydroxyglutamate in IDH-mutated glioma patients by *in vivo* spectral-editing and 2D correlation magnetic resonance spectroscopy. *Sci Transl Med* 2012;4:116ra4.
  129. Choi C, Ganji SK, DeBerardinis RJ, Hatanpaa KJ, Rakheja D, Kovacs Z, et al. 2-hydroxyglutamate detection by magnetic resonance spectroscopy in IDH-mutated patients with gliomas. *Nat Med* 2012;18:624–9.
  130. Andronesi OC, Rapalino O, Gerstner E, Chi A, Batchelor TT, Cahill DP, et al. Detection of oncogenic IDH1 mutations using magnetic resonance spectroscopy of 2-hydroxyglutamate. *J Clin Invest* 2013;123:3659–63.
  131. Tykocinski ES, Grant RA, Kapoor GS, Krejza J, Bohman LE, Gocke TA, et al. Use of magnetic perfusion-weighted imaging to determine epidermal growth factor receptor variant III expression in glioblastoma. *Neuro Oncol* 2012;14:613–23.
  132. Diehn M, Nardini C, Wang DS, McGovern S, Jayaraman M, Liang Y, et al. Identification of noninvasive imaging surrogates for brain tumor gene-expression modules. *Proc Natl Acad Sci U S A* 2008;105:5213–8.
  133. Young RJ, Gupta A, Shah AD, Graber JJ, Schweitzer AD, Prager A, et al. Potential role of preoperative conventional MRI including diffusion measurements in assessing epidermal growth factor receptor gene amplification status in patients with glioblastoma. *AJNR Am J Neuroradiol* 2013;34:2271–7.
  134. Macdonald DR, Cascino TL, Schold SC Jr, Cairncross JG. Response criteria for phase II studies of supratentorial malignant glioma. *J Clin Oncol* 1990;8:1277–80.
  135. Hamstra DA, Chenevert TL, Moffat BA, Johnson TD, Meyer CR, Mukherji SK, et al. Evaluation of the functional diffusion map as an early biomarker of time-to-progression and overall survival in high-grade glioma. *Proc Natl Acad Sci U S A* 2005;102:16759–64.
  136. Ellingson BM, Cloughesy TF, Lai A, Nghiemphu PL, Pope WB. Nonlinear registration of diffusion-weighted images improves clinical sensitivity of functional diffusion maps in recurrent glioblastoma treated with bevacizumab. *Magn Reson Med* 2012;67:237–45.

137. Ellingson BM, Cloughesy TF, Lai A, Mischel PS, Nghiemphu PL, Lalezari S, et al. Graded functional diffusion map-defined characteristics of apparent diffusion coefficients predict overall survival in recurrent glioblastoma treated with bevacizumab. *Neuro Oncol* 2011;13:1151–61.
138. Tsien C, Galban CJ, Chenevert TL, Johnson TD, Hamstra DA, Sundgren PC, et al. Parametric response map as an imaging biomarker to distinguish progression from pseudoprogression in high-grade glioma. *J Clin Oncol* 2010;28:2293–9.
139. Galban CJ, Chenevert TL, Meyer CR, Tsien C, Lawrence TS, Hamstra DA, et al. Prospective analysis of parametric response map-derived MRI biomarkers: identification of early and distinct glioma response patterns not predicted by standard radiographic assessment. *Clin Cancer Res* 2011;17:4751–60.
140. Galban CJ, Chenevert TL, Meyer CR, Tsien C, Lawrence TS, Hamstra DA, et al. The parametric response map is an imaging biomarker for early cancer treatment outcome. *Nat Med* 2009;15:572–6.
141. Kiselev VG, Strecker R, Ziyeh S, Speck O, Hennig J. Vessel size imaging in humans. *Magn Reson Med* 2005;53:553–63.
142. Emblem KE, Mouridsen K, Bjørnerud A, Farrar CT, Jennings D, Borra RJ, et al. Vessel architectural imaging identifies cancer patient responders to anti-angiogenic therapy. *Nat Med* 2013;19:1178–83.
143. Xu C, Kiselev VG, Møller HE, Fiebach JB. Dynamic hysteresis between gradient echo and spin echo attenuations in dynamic susceptibility contrast imaging. *Magn Reson Med* 2013;69:981–91.
144. Pinho MC, Polaskova P, Kalpathy-Cramer J, Jennings D, Emblem KE, Jain RK, et al. Low incidence of pseudoprogression by imaging in newly diagnosed glioblastoma patients treated with cediranib in combination with chemoradiation. *Oncologist* 2014;19:75–81.
145. Shah R, Vattoth S, Jacob R, Manzil FFP, O'Malley JP, Borghesi P, et al. Radiation necrosis in the brain: imaging features and differentiation from tumor recurrence. *Radiographics* 2012;32:1343–59.
146. Verma N, Cowperthwaite MC, Burnett MG, Markey MK. Differentiating tumor recurrence from treatment necrosis: a review of neuro-oncologic imaging strategies. *Neuro Oncol* 2013;15:515–34.
147. Brandes AA, Tosoni A, Spagnoli F, Frezza G, Leonardi M, Calucci F, et al. Disease progression or pseudoprogression after concomitant radiochemotherapy treatment: pitfalls in neurooncology. *Neuro Oncol* 2008;10:361–7.
148. Van Mieghem E, Wozniak A, Geussens Y, Menten J, De Vleeschouwer S, Van Calenberg F, et al. Defining pseudoprogression in glioblastoma multiforme. *Eur J Neurol* 2013;20:1335–41.
149. Brandsma D, van den Bent MJ. Pseudoprogression and pseudoreponse in the treatment of gliomas. *Curr Opin Neurol* 2009;22:633–8.
150. Brandes AA, Franceschi E, Tosoni A, Blatt V, Pession A, Tallini G, et al. MGMT promoter methylation status can predict the incidence and outcome of pseudoprogression after concomitant radiochemotherapy in newly diagnosed glioblastoma patients. *J Clin Oncol* 2008;26:2192–7.
151. de Wit MCY, de Bruin HG, Eijkenboom W, Sillevs Smitt PAE, van den Bent MJ. Immediate post-radiotherapy changes in malignant glioma can mimic tumor progression. *Neurology* 2004;63:535–7.
152. Gerstner ER, McNamara MB, Norden AD, Lafrankie D, Wen PY. Effect of adding temozolomide to radiation therapy on the incidence of pseudo-progression. *J Neurooncol* 2009;94:97–101.
153. Taal W, Brandsma D, de Bruin HG, Bromberg JE, Swaak-Kragten AT, Smitt PAES, et al. Incidence of early pseudo-progression in a cohort of malignant glioma patients treated with chemoradiation with temozolomide. *Cancer* 2008;113:405–10.
154. Gasparetto EL, Pawlak MA, Patel SH, Huse J, Woo JH, Krejza J, et al. Posttreatment recurrence of malignant brain neoplasm: accuracy of relative cerebral blood volume fraction in discriminating low from high malignant histologic volume fraction. *Radiology* 2009;250:887–96.
155. Hu LS, Eschbacher JM, Heiserman JE, Dueck AC, Shapiro WR, Liu S, et al. Reevaluating the imaging definition of tumor progression: perfusion MRI quantifies recurrent glioblastoma tumor fraction, pseudoprogression, and radiation necrosis to predict survival. *Neuro Oncol* 2012;14:919–30.
156. Park I, Tamai G, Lee MC, Chuang CF, Chang SM, Berger MS, et al. Patterns of recurrence analysis in newly diagnosed glioblastoma multiforme after three-dimensional conformal radiation therapy with respect to pre-radiation therapy magnetic resonance spectroscopic findings. *Int J Radiat Oncol Biol Phys* 2007;69:381–9.
157. Li Y, Lupo JM, Parvataneni R, Lamborn KR, Cha S, Chang SM, et al. Survival analysis in patients with newly diagnosed glioblastoma using pre- and postradiotherapy MR spectroscopic imaging. *Neuro Oncol* 2013;15:607–17.
158. Gupta A, Young RJ, Karimi S, Sood S, Zhang Z, Mo Q, et al. Isolated diffusion restriction precedes the development of enhancing tumor in a subset of patients with glioblastoma. *AJNR Am J Neuroradiol* 2011;32:1301–6.
159. Rieger J, Bahr O, Müller K, Franz K, Steinbach J, Hattingen E. Bevacizumab-induced diffusion-restricted lesions in malignant glioma patients. *J Neurooncol* 2010;99:49–56.
160. Van Cauter S, Veraart J, Sijbers J, Peeters RR, Himmelfrich U, De Keyser F, et al. Gliomas: diffusion kurtosis MR imaging in grading. *Radiology* 2012;263:492–501.
161. Kothari PD, White NS, Farid N, Chung R, Kuperman JM, Girard HM, et al. Longitudinal restriction spectrum imaging is resistant to pseudoreponse in patients with high-grade gliomas treated with bevacizumab. *AJNR Am J Neuroradiol* 2013;34:1752–7.
162. Farid N, Almeida-Freitas DB, White NS, McDonald CR, Müller KA, Vandenberg SR, et al. Restriction-spectrum imaging of bevacizumab-related necrosis in a patient with GBM. *Front Oncol* 2013;3:258.
163. Assaf Y, Freidlin RZ, Rohde GK, Basser PJ. New modeling and experimental framework to characterize hindered and restricted water diffusion in brain white matter. *Magn Reson Med* 2004;52:965–78.
164. Jensen JH, Helpert JA, Ramani A, Lu H, Kaczynski K. Diffusional kurtosis imaging: the quantification of non-gaussian water diffusion by means of magnetic resonance imaging. *Magn Reson Med* 2005;53:1432–40.
165. White NS, Leergaard TB, D'Arceuil H, Bjaalie JG, Dale AM. Probing tissue microstructure with restriction spectrum imaging: Histological and theoretical validation. *Hum Brain Mapp* 2013;34:327–46.
166. Panagiotaki E, Schneider T, Siow B, Hall MG, Lythgoe MF, Alexander DC. Compartment models of the diffusion MR signal in brain white matter: a taxonomy and comparison. *Neuroimage* 2012;59:2241–54.
167. Correia Carreira G, Gemeinhardt O, Gorenflo R, Beyersdorff D, Franiel T, Plendl J, et al. Limitations of the permeability-limited compartment model in estimating vascular permeability and interstitial volume fraction in DCE-MRI. *Magn Reson Imaging* 2011;29:639–49.
168. Hassid Y, Furman-Haran E, Margalit R, Eilam R, Degani H. Noninvasive magnetic resonance imaging of transport and interstitial fluid pressure in ectopic human lung tumors. *Cancer Res* 2006;66:4159–66.
169. Pellerin M, Yankeelov TE, Lepage M. Incorporating contrast agent diffusion into the analysis of DCE-MRI data. *Magn Reson Med* 2007;58:1124–34.
170. Yankeelov TE, Rooney WD, Huang W, Dyke JP, Li X, Tudorica A, et al. Evidence for shutter-speed variation in CR bolus-tracking studies of human pathology. *NMR Biomed* 2005;18:173–85.
171. Carreira GC, Gemeinhardt O, Gorenflo R, Beyersdorff D, Franiel T, Plendl J, et al. Limitations of the permeability-limited compartment model in estimating vascular permeability and interstitial volume fraction in DCE-MRI. *Magn Reson Imaging* 2011;29:639–49.
172. Mills SJ, Soh C, Rose CJ, Cheung S, Zhao S, Parker GJ, et al. Candidate biomarkers of extravascular extracellular space: a direct comparison of apparent diffusion coefficient and dynamic contrast-enhanced MR imaging-derived measurement of the volume of the extravascular extracellular space in glioblastoma multiforme. *AJNR Am J Neuroradiol* 2010;31:549–53.
173. Paulson ES, Schmainda KM. Comparison of dynamic susceptibility-weighted contrast-enhanced MR methods: recommendations for measuring relative cerebral blood volume in brain tumors. *Radiology* 2008;249:601–13.